MODELING DESICATION CRACKS IN OPALINUS CLAY AT FIELD SCALE WITH THE PHASE-FIELD APPROACH

Tuanny Cajuhi[1] (iD), Gesa Ziefle[1] (iD), Jobst Maßmann[1] (iD), Thomas Nagel[2] (iD), Keita Yoshioka[3] (iD)

[1]*Federal Institute for Geosciences and Natural Resources (BGR), Geotechnical Safety Analyses, Hannover, Germany;* [2]*Technische Universität Bergakademie Freiberg, Geotechnical Institute, Freiberg, Germany;* [3]*Montanuniversität Leoben, Department Geoenergy, Leoben, Austria*

ABSTRACT

Geological materials such as Opalinus Clay show complex coupled hydro-mechanical behavior at laboratory and field scales. In the context of radioactive waste disposal, in-situ excavations might remain open for ventilation and operation for decades and, consequently, be susceptible to environmental changes such as desaturation. The saturation changes can then lead to mechanical deformation and desiccation cracks. To account for desiccation cracking at field scale, this study proposes an unsaturated hydro-mechanical model combined with the phase-field approach. Using laboratory and in-situ experimental data as input in the numerical model, the modeling framework is applied for simulating the hydro-mechanical effects and desiccation cracks reported in the Cyclic Deformation (CD-A) experiment carried out in the Opalinus Clay formation at the Mont Terri Rock Laboratory in Switzerland. Simulations with homogeneous and heterogeneous material properties generated from experimentally obtained ranges are carried out. Crack initiation and propagation show a good correlation with the monitored relative humidity range of the experiment. Practical information is summarized to motivate the application of the proposed formulation at different setups. Finally, possibilities to improve the framework and to reason simplification of more abstract models are indicated.

1. INTRODUCTION

In the context of radioactive waste disposal, clayey materials such as Opalinus Clay are considered as potential host rocks or geological and geotechnical barriers. The integrity of these barriers, i.e. their ability to fulfill safety functions, needs to be maintained during all phases from repository construction to operation and post-closure. To this end, their mechanical and fracture behaviors need to be

thoroughly studied and understood. In-situ excavations can be used once they are considered stable (41). During their construction and/or operation, they are open and susceptible to environmental changes such as the influence of relative air humidity and temperature (41, 42). These changes can be caused by seasonal and climatic conditions, which may re-distribute the near-field stress and become more dominant than the initial in-situ conditions in this region. Consequently, they can facilitate or hinder the development of existing cracks. When the walls of the excavated region desaturate, the rock expels pore water and consequently contracts. This volume reduction is called shrinkage and causes strain gradients in the rock. As a result of these gradients and restraints, shrinkage-induced (or desiccation) cracks can nucleate (14, 62, and references therein). However, the (re)saturation of the material, i.e. an increase in the liquid content, is associated with bulk expansion and can lead to crack closing (62, 78, 80)[1].
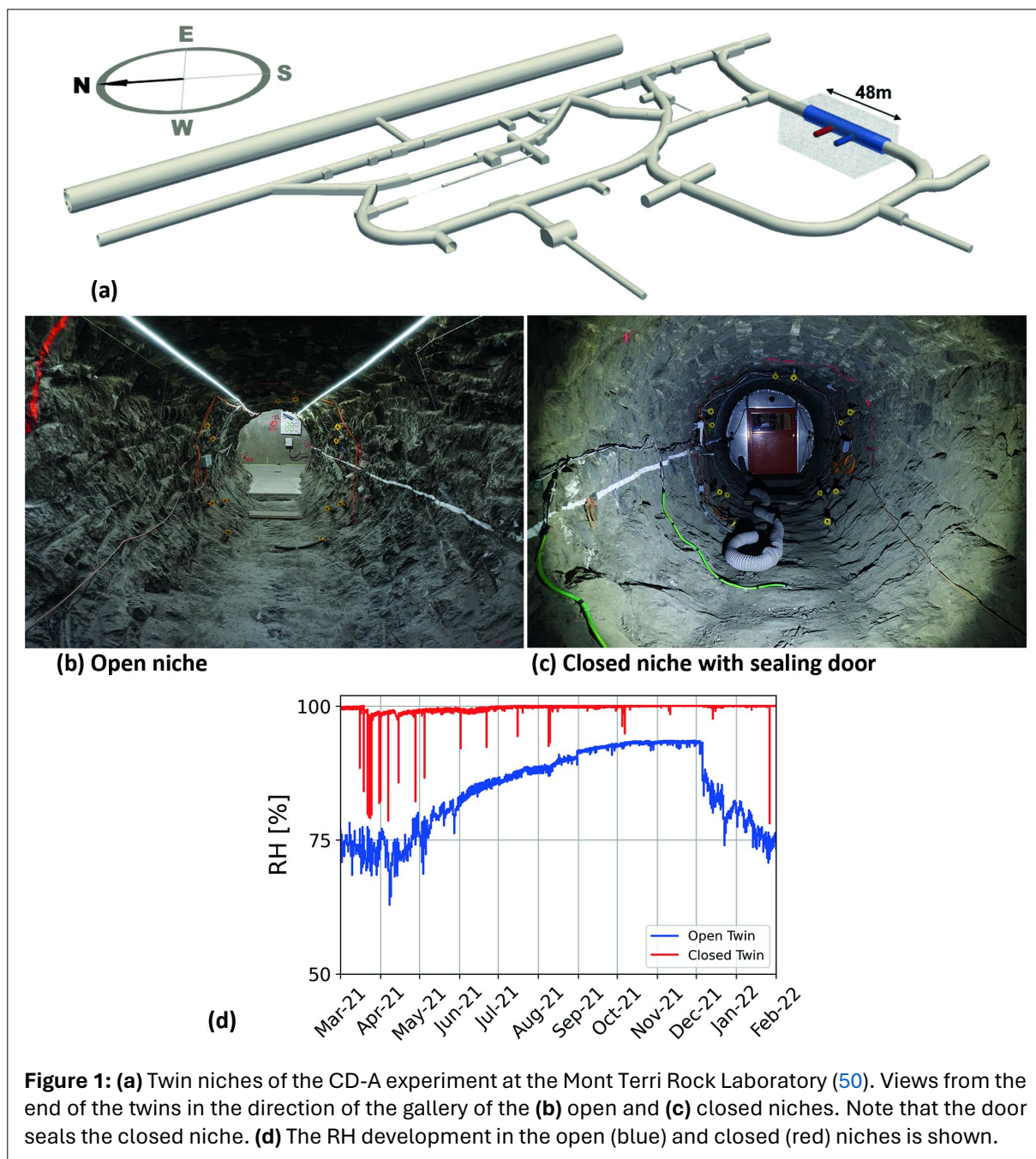
Figure 1: (a) Twin niches of the CD-A experiment at the Mont Terri Rock Laboratory (50). Views from the end of the twins in the direction of the gallery of the **(b)** open and **(c)** closed niches. Note that the door seals the closed niche. **(d)** The RH development in the open (blue) and closed (red) niches is shown.

---

[1] *The expression "crack closing" can either be associated with the recovery of the hydraulic behavior,* e.g. *permeability is recovered (sealing), and/or of the mechanical integrity (healing).*

The aforementioned interactions are summarized in coupled hydro-mechanical behavior, e.g. capillary actions, changes in pore pressure, and fluid content due to variations in humidity, material response to strains, and stresses, among others. They can significantly impact the mechanical properties, strength, and failure behavior of porous materials/geomaterials, such as clayey rocks. In summary, understanding the hydro-mechanical behavior is crucial as it dictates how materials such as Opalinus Clay respond to changes in moisture content and external loads, which has direct consequences for the safety and performance of radioactive waste disposal sites. This coupled hydro-mechanical behavior is observed in both laboratory and in-situ experiments (18, 43, 71, 72, 86). However, in the latter, the temporal and spatial scales are much larger than those in the laboratory. The Cyclic-Deformation (CD-A) experiment (82, 83, 85) carried out in the Rock Laboratory Mont Terri (7) in an Opalinus Clay formation in Switzerland (**Fig. 1a**) focuses on understanding coupled hydro-mechanical effects by comparing the response of two identical (twin) niches to the excavation and ventilation conditions. The twin niches have a diameter of 2.3 m and a length of approximately 11 m. They are oriented perpendicular to the strike of the bedding and have no stabilization support (e.g. shotcrete or steel arches). Nevertheless, to date, the excavated twins have shown no indication of integrity loss due to desiccation cracks since the experiment and geophysical measurements started in October 2019. The twins are shown in **Figure 1b-c**. The open niche or "natural twin" is shown in **Figure 1b**. Its relative air humidity (RH) varies with the ventilation of the gallery and is therefore affected by seasonal fluctuations, as depicted by the blue curve in **Figure 1d**. The closed twin was sealed with a door, as shown in **Figure 1c**. The RH remained relatively constant (red curve in **Fig. 1d**).

Both twins are equipped with a large number of sensors that provide data for detailed characterization of the host rock. The measurements include electrical resistivity, lithologic description, transmissibility,

Figure 2: Open niche with **(a)** drawn scanline and **(b)** monitored RH and sum of crack apertures of cracks measured at the scanline intersection. Note that cracking becomes more intense once the rock desaturates, i.e. the relative humidity decreases (plot based on the results from [53]).
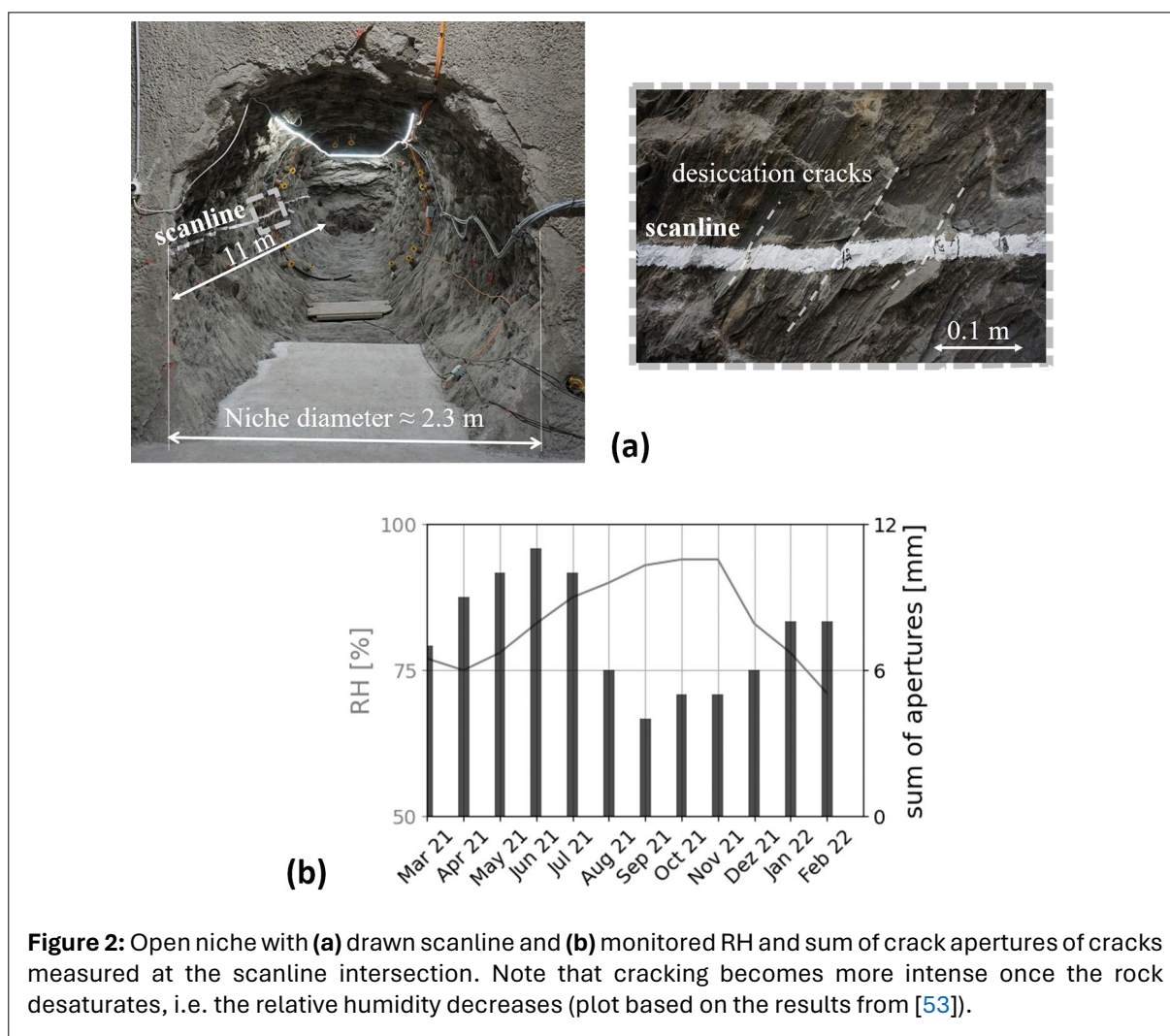
and observation of important process variables such as convergence (84), relative humidity, water content (83, 84), suction, and crack development (16). Furthermore, the geological conditions were investigated by detailed lithological and structural mapping of several core probes and niches, both during and after the excavation phase.

In this paper, we focus on the open niche, where the effects of desaturation, as emphasized by humidity changes and consequent cracking, are more pronounced when compared to the closed twin. **Figure 2a** shows the open niche and the white scanline used to monitor crack development. The scanline was drawn horizontally, approximately in the middle of the niche and along its length. Its basic idea was to ease the identification of cracks in heterogeneous rock and to observe the evolution of crack parameters, such as vertical length/extension, aperture width, and the distance between the cracks. The scanline procedure and results are described in (53), which shows that more than 90% of the drying cracks propagate parallel to the bedding. The monitored results obtained during the summer and winter of 2021 are shown in **Figure 2b**. Note that cracking becomes more intense during the drying winter months, as indicated by the increase in the sum of the crack apertures. The reverse, that is, a decrease in the sum of the crack apertures, is observed during summer with re-saturation.

Because of the complexity of the ongoing processes in the desaturating niche, experimental knowledge must be complemented by numerical models. Mathematical and numerical modeling play an important role in understanding the coupled behavior and effects at different scales, especially when long-term behavior is of interest. The reported coupled rock behavior, i.e. hydro-mechanical interactions that can lead to fracture, requires multi-field mathematical and numerical approaches, i.e. accounting for interconnected physical processes, to simulate and understand the complex rock behavior, as reported in the literature (35, 57). Because rocks can often be idealized as porous materials, poromechanical theories are widely used to describe non-fractured media (57, 87). These established theories have been applied in different contexts and materials (17, 25, 52, 55, 57, 86) and have been validated against experimental data at the laboratory scale (14). To account for cracking, poromechanical approaches can be combined with discrete and continuous crack-modeling frameworks (15, 17, 19, 27, 32, 49, 58, 73). Crack modeling approaches such as discrete modeling, remeshing and extended Finite Element require additional criteria and/or inclusion of "weaker" points in the domain to induce crack initiation. Furthermore, crack propagation needs to be tracked. The phase-field approach is advantageous in this regard because it enables crack nucleation and propagation without the need for ad hoc criteria. This has proven to be a good alternative when dealing with desiccation cracks at the laboratory scale (17, 28, 39) since these can nucleate at any point in a domain. In the aforementioned literature, a hydro-mechanical model was combined with the phase-field model for brittle fracture and applied at the laboratory scale. The porous media assumptions are customary, and the basic difference between them concerns the coupling, i.e. degradation of the effective or total stress. Further desiccation modeling approaches that are not related to the phase field are summarized in a review paper (63). To the best of the authors' knowledge, the amount of literature in which the phase-field approach is developed and used in modeling cracks at a large field scale is rather scarce. The Callovo-Oxfordian (COx) formation has been used in several studies (69, 70, 77). In (77), the hydro-mechanical response of an excavation is evaluated using two damage fields (phase-field evolution equations) that differentiate between the tensile and shear contributions. In (69, 70), the swelling effects and self-sealing of cracks around an excavation were investigated. The aforementioned approaches focus on saturated porous media[2]; consequently, cracks due to drying/desiccation are not the main objective of this study and are not considered. The present study aims to apply the laboratory-scale method developed in (14, 17) for clay soils and cement-based materials at the field scale for the Opalinus Clay formation. These investigations were conducted during a joint research project (36).

1.1.   **Aims and outline**

In this study, we aim to increase the understanding of the process of cracking due to desiccation in Opalinus Clay at the field scale. For this purpose, the coupled hydro-mechanical-phase-field approach

---

[2] In (44) partial saturation is taken into account for modeling rainfall-induced landslides within a hydro-mechanical phase-field approach that differentiates between tensile and shear contributions.

(17) developed for clay soils and validated against laboratory experiments with cementitious materials has been extended to two popular phase-field models known as AT_1 and AT_2 models, and to a more flexible irreversibility implementation. Then, the method is applied at the in-situ scale to model desiccation cracks of the Opalinus Clay formation in Mont Terri. The present study and implementation were carried out in the context of the joint research project "Geomechanical integrity of host and barrier rocks - experiment, modeling, and analysis of discontinuities (GeomInt2)" (36). The reader is referred to (15) (in [36]) for an overview of general aspects regarding hydro-mechanical and cracking effects in Opalinus Clay at laboratory and field scales. Regarding the aforementioned references, examples of crack pattern formation in a three-dimensional setting were investigated with respect to their mechanical boundary conditions. Consequently, it refers to a preliminary proof-of-concept, where the deduction of the fracture properties and the formal steps for applying the framework at the in-situ scale are not considered. The present study focuses on understanding the conditions under which cracks initiate, as well as how deep they propagate. This is an important step in confirming safety requirements and simplifying more abstract/less detailed models in the context of long-term safety analyses and performance assessments. The necessary ingredients for applying the framework are summarized, and experimental data are used as the basis for the determination of the material parameters and input for the boundary conditions. We show the crack evolution with respect to the pore pressure, strain, and strain energy evolution, as well as the effect of local changes in permeability with monitored cracking and relative humidity at the field scale. The distinct aspects and highlights of this study are summarized as follows:

- Adaptation of a framework that has been used only at the laboratory scale to the field scale.
- Direct parameterization and practical interpretation of the proposed numerical framework for field-scale applications in Opalinus Clay.
- The simulated crack initiation and propagation lie within the in situ-monitored relative humidity range.
- Demonstration of enhanced desaturation through coupling of the damaged zone and locally increased permeability in the crack.
- Impact of randomly distributed material properties (permeability, porosity, and fracture energy) on crack propagation.

The governing equations and implementation of the framework as well as its limiting assumptions are described in Section 2. The numerical model was implemented using open-source software OpenGeoSys (5, 35, 36). In Section 3, the required material properties and the deduction of fracture parameters using the phase-field approach are discussed. The hydro-mechanical effects followed by the crack response are discussed stepwise while using the complete framework in a homogeneous test case. The starting point for the numerical simulations was stable open excavation. The development of stresses that occur after excavation-induced effects owing to desiccation was considered. Further, test cases using random fields were considered. Finally, the results and application steps are summarized in Section 4 and the main conclusions are discussed in Section 5.

2. GOVERNING EQUATIONS

Consider a porous medium in $\Omega \in \mathbb{R}^N$ with a crack set $\Gamma \in \mathbb{R}^{N-1}$. We computed the liquid pore pressure changes and deformation based on the hydro-mechanical coupled model proposed in (37, 55, 87). In such macroscopic poromechanical approaches, porous media are considered at a scale where individual pores are not explicitly modeled; instead, average, or effective properties such as porosity, effective stress, and saturation are used to describe the behavior of the entire medium. The porous medium is conceptualized as a continuum comprising two interpenetrating continua: solid matrix and pore space. The solid matrix represents the grains or solid skeleton of the material, while the pore space represents the voids or gaps between these grains where fluids can reside and apply a variational phase-field approach to account for shrinkage-induced cracking. The governing equations presented in the following are based on an isothermal unsaturated approach, discretized with a Bubnov-Galerkin Finite

Element Method, and implemented in the open-source software OpenGeoSys (4, 5, 33, 35, 36). The algorithmic implementation of the poromechanical equations follows the approach as described in (52).

2.1.   Mass balance equation of pore fluid

The porous medium consists of fluid $(\cdot)_F$ and solid $(\cdot)_S$ phases. The fluid that fills the pore space is comprised of gas $(\cdot)_G$ and liquid $(\cdot)_L$ components. The degree of saturation $S_\propto$ is required to identify the amount of each fluid phase $\propto$ in pore space, such that $S_L + S_G = 1$. The pore pressure p_F was computed as a weighted average of the phase pressures, as shown in **Equation 1** where p_L and p_G are the liquid and gas pressures, respectively.

$$p_F = S_L p_L + (1 - S_L) p_G \tag{1}$$

In the description of variably saturated flow, we employed the Richards approximation (54) (**Eq. 2**) where p_{cap} develops when the medium desaturates and is computed at reference gas pressure $p_G = 0$. Due to this assumption and for further simplicity, we use the terms pore pressure and pressure interchangeably to refer to the liquid pore pressure. For the same reason, the term saturation refers to the liquid phase.

$$\begin{aligned} p_{cap} &= p_G - p_L \\ &= -p_{L,} \end{aligned} \tag{2}$$

Since the mathematical values corresponding to full saturation $S_L = 1$ and complete desaturation $S_L = 0$ are not reached under practically relevant boundary conditions, the effective saturation S_{eff} is defined by **Equation 3**, where $S_{L,res}$ and $S_{L,max}$ are the residual and maximum saturations in the medium, respectively.

$$S_{eff} = \frac{S_L - S_{L,res}}{S_{L,max} - S_{L,res}} \tag{3}$$

Water retention curves were obtained experimentally and represented the relationship between moisture content and relative humidity in the medium. These curves can be re-plotted in terms of saturation and pressure and fitted with solid liquid retention curves (12, 22, 68). In this work, we use the van Genuchten law (68) given by **Equation 4** where p_b is related to the air entry value and m is associated with the shape factor/pore size distribution (68).

$$S_{eff} = \left(1 + \left(\frac{p_{cap}}{p_b} \right)^{\frac{1}{1-m}} \right)^{-m} \tag{4}$$

Similar to saturation, the van Genuchten model was applied to compute the relative permeability $k_{rel}(S_L)$ as shown in **Equation 5**:

$$k_{rel} = \sqrt{S_{eff}} \left(1 - \left(1 - S_{eff}^{\frac{1}{m}} \right)^{2m} \right) \tag{5}$$

Many geological formations considered for radioactive waste disposal, such as Opalinus Clay, exhibit low permeability. This characteristic implies that the pore spaces between the grains are either small or poorly interconnected, which restricts the fluid flow through the rock. As a result, one can expect low flow velocities, leading to a typically low Reynolds number indicative of laminar flow. This assumption was made in our study. However, it is important to note that the flow regime might shift if cracks develop within the rock matrix, which is not accounted for in the present study. The relative velocity of the fluid with respect to the solid averaged over the porous medium area elements can be computed using Darcy's law (**Eq. 6**). The velocity of the liquid is affected by $k_{rel}(S_L)$, the intrinsic permeability tensor of the medium $\mathbf{K}$, the dynamic viscosity of the liquid μ_L, the gradient of the pressure, the specific body force $\mathbf{b}$, and the density of the liquid ρ_L.

$$\widetilde{\mathbf{w}}_L = -\frac{k_{rel}(S_L)\mathbf{K}}{\mu_L}(\nabla p_L - \rho_L \mathbf{b}) \tag{6}$$

Assuming a constant liquid density and incompressible solid grains, the mass balance equation of the pore fluid is computed taking into account the rate of liquid flow (**Eq. 6**), and the accumulation terms, as in **Equation 7** where ϕ is the porosity and $\nabla^s \mathbf{u} = \frac{1}{2}(\nabla \mathbf{u} + \nabla \mathbf{u}^T)$ is the symmetric small-strain tensor. The second term of **Equation 7** represents the temporal variation in liquid storage. The last term of this equation accounts for volume changes in the porous medium. Note again that the liquid and solid grains are considered to be intrinsically incompressible, and for this reason, further accumulation terms related to liquid or solid grain density changes are not considered here but are available as part of the process model in OpenGeoSys ([17], [26], [33], [87]). The boundary conditions are implemented with fixed pressure $\bar{p}_L$ or mass flux $\bar{q}$.

$$\nabla \cdot (\rho_L \widetilde{\mathbf{w}}_L) + \rho_L \phi \frac{\partial S_L}{\partial t} + \rho_L S_L \frac{\partial \text{tr}(\nabla^s \mathbf{u})}{\partial t} = 0 \text{ in } \Omega \tag{7}$$

$$p_L = \bar{p}_L \text{ on } \partial\Omega_D^p$$

$$\rho_L \widetilde{\mathbf{w}}_L \cdot \mathbf{n} = \bar{q} \text{ on } \partial\Omega_N^p$$

2.2.   Mechanical equilibrium conditions

The equilibrium equation is computed in a standard manner with the total stress $\boldsymbol{\sigma}$ and specific body forces $\mathbf{b}$ using **Equations 8** to **11**, and with average density $\rho = \phi S_L \rho_L + (1 - \phi)\rho_S$.

$$-\nabla \cdot \boldsymbol{\sigma} = \rho \mathbf{b} \text{ in } \Omega \setminus \Gamma \tag{8}$$

$$\mathbf{u} = \bar{\mathbf{u}} \text{ on } \partial\Omega_D^u \tag{9}$$

$$\boldsymbol{\sigma} \cdot \mathbf{n} = \bar{\mathbf{t}} \text{ on } \partial\Omega_N^u \tag{10}$$

$$\boldsymbol{\sigma} \cdot \mathbf{n}_\Gamma = -\alpha S_L p_L \mathbf{n}_\Gamma = \mathbf{0} \text{ on } \Gamma \tag{11}$$

To explicitly account for all phases, the total stress is split into the effective stress $\boldsymbol{\sigma}_{\text{eff}}$, and the pore pressure α represents the Biot coefficient (**Eq. 12**).

$$\boldsymbol{\sigma} = \boldsymbol{\sigma}_{\text{eff}} - p_F \mathbf{I} = \boldsymbol{\sigma}_{\text{eff}} - \alpha S_L p_L \mathbf{I} \tag{12}$$

The effective stress is given by **Equation 13** where $\mathbb{C}$ is the elastic stiffness tensor.

$$\boldsymbol{\sigma}_{\text{eff}} = \mathbb{C} : \boldsymbol{\varepsilon}(\mathbf{u}) \tag{13}$$

In the next section, we couple the poromechanical part of the framework with the phase-field model, where we provide further details on the computation of $\mathbb{C}$. The computation of the strain energy for the volumetric-deviatoric split is discussed in **Appendix A** (available to download online).

2.3.   Crack phase-field evolution

The derivation of the crack phase-field evolution equation of brittle fracture follows the general approach in the literature, where the free-energy functional is minimized and leads to a variational regularized energy functional ([1], [9]). Phase-field models for brittle fracture are based on the regularization of the free energy functional form ([20]), as shown in **Equation 14** where G_c is the fracture energy and dS is the portion of the boundary associated with the crack (crack set).

$$\text{E}(\mathbf{u}, \Gamma) := \mathcal{P}(\mathbf{u}) + \int_\Gamma G_c dS \tag{14}$$

Without body forces and external loading, the potential energy $\mathcal{P}(\mathbf{u})$ is given by ([74]) **Equation 15** where Ψ is the strain energy density given as shown in **Equation 16**.

$$\mathcal{P}(\mathbf{u}) = \int_{\Omega \setminus \Gamma} \Psi(\mathbf{u}) d\Omega - \int_{\Omega \setminus \Gamma} \boldsymbol{\varepsilon}(\mathbf{u}) : (p_F \mathbf{I}) d\Omega \tag{15}$$

$$\Psi(\mathbf{u}) = \frac{1}{2} \boldsymbol{\varepsilon}(\mathbf{u}) : \mathbb{C} : \boldsymbol{\varepsilon}(\mathbf{u}) \tag{16}$$

Bourdin *et al.* (8) proposed regularizing this energy functional following (47) by introducing a phase-field variable $d \in [0, 1]$, which varies from intact $d = 0$ to fully broken $d = 1$, and a regularization length parameter ℓ as shown in **Equation 17** where $\mathcal{P}(d, \mathbf{u})$ is a regularized strain energy density with degradation of the effective stress i.e. **Equation 18,** as proposed in (17, 29).

$$E_\ell(\mathbf{u}, d) \coloneqq \mathcal{P}(d, \mathbf{u}) + \int_\Omega \frac{G_c}{4c_w}\left(\frac{w(d)}{\ell} + \ell|\nabla d|\right) d\Omega \tag{17}$$

$$\mathcal{P}(d, \mathbf{u}) = \int_\Omega \Psi(d, \mathbf{u}) d\Omega - \int_{\Omega\backslash\Gamma} \boldsymbol{\varepsilon}(\mathbf{u}) : (p_F \mathbf{I}) \, d\Omega + \int_{\Omega\backslash\Gamma} \frac{(p_F)^2}{6K} d\Omega \tag{18}$$

The second integral represents the regularized crack surface with **Equation 19** where $n = 1$ and 2 stand for so-called AT_1 and AT_2 models respectively (10, 51), and $c_w = 2/3$ for AT_1 and $1/2$ for AT_2 (45, 65).

$$w(d): d^n \text{ and } c_w \coloneqq \int_0^1 (1-s)^{n/2} ds \tag{19}$$

For the regularized potential energy, $\mathcal{P}(d, \mathbf{u})$, following (17, 28), we decomposed it into an active Ψ_+ and an inactive part Ψ_-, and only degrade the elastic part of the potential energy (Ψ) (**Eq. 20**):

$$\Psi(d, \mathbf{u}) = g(d)\Psi_+(\mathbf{u}) + \Psi_-(\mathbf{u}) \tag{20}$$

The degradation function $g(d)$ is computed with **Equation 21** where η is the (small) residual stiffness assigned for numerical stability for fully broken parts $d = 1$ (e.g. $\eta = 10^{-8}$). The strain energy decomposition is an important ingredient in the phase-field formulation (2, 21, 38, 67). In this study, we used the volumetric-deviatoric strain energy decomposition (2) with AT_1 formulation. The derivations are reported in **Appendix A** (available to download online).

$$g(d) = (1 - d)^2 + \eta \tag{21}$$

The first variation of **Equation 17** with respect to $\boldsymbol{\varepsilon}(\mathbf{u})$ leads to the momentum balance equation (**Equation 8**) with degraded effective stress in the form of **Equation 22** where $\boldsymbol{\sigma}_{\text{eff},\pm} = \partial\Psi_\pm/\partial\boldsymbol{\varepsilon}$ depends on the chosen strain energy decomposition (**App. A,** available to download online) and consequently affects the stiffness tensor (**Eq. 23**).

$$\boldsymbol{\sigma}_{\text{eff}} = g(d)\boldsymbol{\sigma}_{\text{eff},+} + \boldsymbol{\sigma}_{\text{eff},-} \tag{22}$$

$$\mathbb{C}(d) = g(d)\mathbb{C}_+ + \mathbb{C}_- \tag{23}$$

$$= g(d)\frac{\partial^2\Psi_+}{\partial\boldsymbol{\varepsilon}^2} + \frac{\partial^2\Psi_-}{\partial\boldsymbol{\varepsilon}^2}$$

Note that, in the present framework, the degradation function was applied to the effective stress. Another possibility currently being investigated is the degradation of total stress. As shown in **Equation 12**, Biot's coefficient α is an important parameter that correlates the effective stress and pore pressure. This coefficient is related to the Bulk modulus of the porous medium K_D and of the solid K_S via the relation $\alpha = 1 - K_D/K_S$ (30). Once the porous material is degraded, its stiffness (and consequently its bulk modulus) decreases and the porosity increases. Multiplying the degradation function to the total stress would, consequently, introduce a similar dynamic to the model. However, it is necessary to evaluate this step critically, i.e. how much of such a degradation should be applied to the total stress, since a full degradation seems rudimentary. Another feature of a total stress degradation is the possibility of modifying the traction boundary condition acting on the crack faces. In other words, one can distinguish liquid-saturated cracks (as in hydraulic fracturing) with $\boldsymbol{\sigma} \cdot \mathbf{n}_\Gamma = -p_L\mathbf{n}_\Gamma$ from cracks filled with water vapour at reference pressure, where traction-free conditions prevail, $\boldsymbol{\sigma} \cdot \mathbf{n}_\Gamma = \mathbf{0}$. Thus, a total stress degradation would be linked to additional conditions, such as the fluid content of the crack and should not be done blindly.

The first order optimality of **Equation 17** with respect to d yields the phase-field evolution equation as shown in **Equation 24**.

$$g^{'}(d)\Psi_+(\mathbf{u}) + \frac{G_c}{4c_w}\left(\frac{w^{'}(d)}{\ell} + 2\ell\Delta d\right) = 0 \tag{24}$$

The fluid pressure term is not present in **Equation 24**, because only the effective stress is degraded in the potential energy form (**Eq. 18**). In the proposed unsaturated modeling approach, cracks are assumed to fill with gas at the reference pressure and are thus considered load-free (**Eq. 11**). Owing to the weak coupling between the liquid pressure and crack phase field in this study, crack initiation did not lead to enhanced drying, i.e. the additional crack edges/surfaces did not act as drying boundaries in the framework. In solving **Equation 24**, we have the constraint that damage evolution is irreversible, i.e. its time derivative must be positive all the time, $\dot{d} > 0$. To implement irreversibility, we discuss the different options in the following section.

2.4.   Implementation

The numerical treatment of **Equations 7**, **8**, and **24** is based on the standard Bubnov-Galerkin finite element method. The equations were linearized using the Newton-Raphson method. Framework (33) was implemented in OpenGeoSys (4, 5, 35, 36). The implementation resulted in a process called the *Richard mechanics phase field*.

The solution scheme is divided into two sub-problems. In the first sub-problem, the hydro-mechanical part is solved for the variables $\mathbf{u} - p_L$. Strongly coupled variables were solved using a monolithic approach. During the solution of $\mathbf{u} - p_L$, the crack phase-field d remains frozen. The second subproblem consists of solving the phase-field evolution equation for d during which the $\mathbf{u} - p_L$ pair is kept frozen. In this way, the subproblems are solved within a staggered approach up to convergence. A schematic representation of the solution scheme is shown in **Figure 3**. This hybrid scheme allows us to combine the strengths of each subproblem solution, i.e the robustness of a monolithic scheme for $\mathbf{u} - p_L$ and the flexibility to integrate a further evolution equation as the one driving d when using a staggered approach. The general algorithmic form of the hybrid solution is shown in (14, 17). Furthermore, the time is discretized with the backward Euler scheme.

A further relevant aspect in the implementation is the choice of element type. To satisfy the Ladyzhenskaya-Babuska-Brezzi (LBB) condition, we chose Taylor-Hood elements with a quadratic

Figure 3: Simplified flowchart of hybrid solution scheme showing the connection between the monolithic ($\mathbf{u}, \boldsymbol{p_L}$) and staggered ($\boldsymbol{d}$) solutions. The phase-field solution requires a variational inequality solver to satisfy the irreversibility condition in **Equation 27**. During initialization, the initial boundary conditions are assigned.
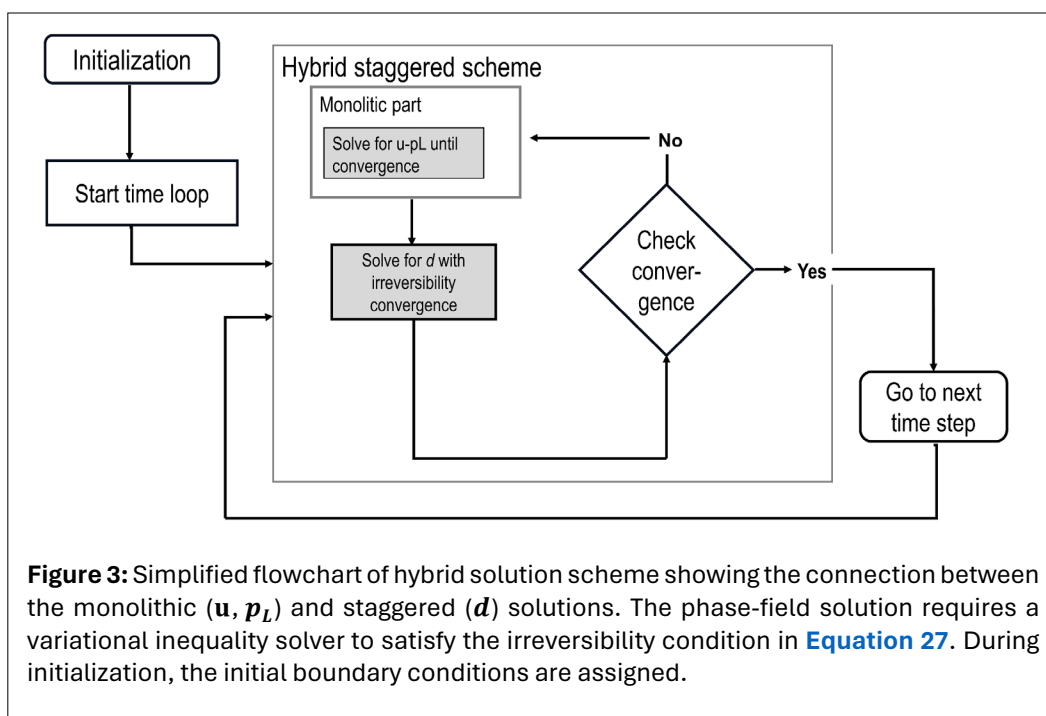
interpolation order for the displacement and linear order for the pore pressure (87). The crack phase-field variable is interpolated with linear elements. Previous work on desiccation-induced cracking reported that the interpolation order of the crack phase-field (quadratic/linear) only affects the position of the crack initiation and not the amount and quality of the cracks (14).

Note that the unsaturated hydro-mechanical problem is rate-dependent, and thus, given appropriate boundary conditions, the crack evolution also becomes rate-dependent. The solution space is obtained using **Equation 25** where $\mathcal{U}$ is the kinematically admissible displacement set (**Eq. 26**), and the admissible set of d is **Equation 27**, where d_{irr} is a variable that controls the irreversibility (8, 13).

$$(\mathbf{u}_i, d_i) = \arg\min\{\mathcal{E}_\ell(\mathbf{u}, d) : \mathbf{u} \in \mathcal{U}(t_i), d \in \mathcal{D}(t_i, d_{i-1})\} \tag{25}$$

$$\mathcal{U}(t_i) = \{\mathbf{u} \in H^1(\Omega) : \mathbf{u} = \overline{\mathbf{u}} \text{ on } \partial\Omega_\mathrm{D}^u\} \tag{26}$$

$$\mathcal{D}(t_i, d_{i-1}) = \{d \in H^1(\Omega) : 0 \le d_{i-1}(x) \le d(x) \le 1 \forall x \text{ s.t. } d_{i-1}(x) \ge d_{\mathrm{irr}}\} \tag{27}$$

If we set a small d_{irr} (e.g., $d_{\mathrm{irr}} = 0.01$), the damage is irreversible in a strict sense. On the other hand, if we set a large d_{irr} (e.g., $d_{\mathrm{irr}} = 0.99$), the modeled damage is reversible until complete failure of the material and the crack can seal/heal. In this study, we refer to the first setting as "hard" irreversibility and the latter as "soft" irreversibility. Consequently, we must solve d with an inequality constraint, which is achieved through the variational inequality solver provided by PETSc (3). The accuracy of the model was verified using the Liakopoulos benchmark (hydro-mechanical part) and constrained Liakopoulos (17). Furthermore, the results of the implemented framework showed good agreement with the desiccation test results at the laboratory scale performed by others (17, 60).

3. APPLICATION AT FIELD SCALE

The effects of desaturation and deformation are monitored regularly in the CD-A experiment. Desaturation is driven by a decrease in relative humidity and occurs seasonally, particularly during winter, resulting in desiccation cracks in the near field of the open niche. None of the excavated twins have shown integrity loss due to desiccation cracks since the experiment and geophysical measurements started in October 2019. For this reason and to keep the modeling as simple as possible, the starting point of the numerical model is chosen to be after the instant stress redistribution due to excavation, i.e. the stable, open excavation (open niche). The desiccation effects superimpose the excavation-induced stress redistribution in the near field. Therefore, the initial effects do not play a critical role in the desiccation phenomenon addressed in this study. Consequently, only the changes in the stresses after the instant stress redistribution are modelled. The inclusion of excavation related effects is planned to be investigated in further studies, where the damage due to the excavation will be interpreted as initial boundary condition for the crack phase-field. Another ongoing and important study is the consideration of the mechanical and hydraulic anisotropy that can influence crack orientation.

3.1.   Material parameters

For modeling the CD-A experiment, we collected the material properties corresponding to the sandy facies of the Opalinus Clay (6, 7, 24, 79) where the niches are located (34, 83). The properties are summarized in **Table 1**. Note that we also determined the so-called isotropic equivalent properties as the average of each anisotropic quantity, for example, the isotropic equivalent of the elastic modulus is the average of the two parallel and transverse components. The fracture related properties, e.g. fracture toughness and tensile strength, as well as the Biot parameter were obtained from (6, 30) and correspond to the Mont Terri region, which comprises not only sandy, but also shaly and carbonate-rich facies (6, 33). The reported parameters are used for the deduction of the crack phase-field-related quantities.

Table 1: Parameters and material properties for modeling the CD-A experiment. Subscript 1 denotes the transversal component, while subscript 2 and 3 denote the parallel ones. The isotropic equivalent properties are computed by averaging the anisotropic properties.

Parameter	Symbol	Value
Liquid density	ρ_L	$1000 \, \mathrm{kg} \cdot \mathrm{m}^{-3}$
Dynamic viscosity	μ_L	$1.0 \cdot 10^{-3} \, \mathrm{Pa} \cdot \mathrm{s}^{-1}$
Solid grain density	ρ_S	$2520 \, \mathrm{kg} \cdot \mathrm{m}^{-3}$
Porosity	ϕ	0.105
Biot coefficient	α	1
Intrinsic permeability	K_1 K_2, K_3	$0.4 \cdot 10^{-19} \, \mathrm{m}^2$ $1.0 \cdot 10^{-19} \, \mathrm{m}^2$
Gas entry pressure	$\mathrm{p_b}$	$10.0 \cdot 10^6 \, \mathrm{Pa}$
Shape factor	m	0.45
Residual saturation	S_r	0.10
Elastic modulus	E_1 E_2, E_3	$6.0 \cdot 10^9 \, \mathrm{Pa}$ $13.8 \cdot 10^9 \, \mathrm{Pa}$
Poisson's ratio	ν_{12}, ν_{13} ν_{23}	0.22 0.44
Shear modulus	G_{12}, G_{13}	$3.2 \cdot 10^9 \, \mathrm{Pa}$
Fracture toughness	$K_{\mathrm{I}1}$ $K_{\mathrm{I}2}, K_{\mathrm{I}3}$	$0.12 \pm 0.03 \, \mathrm{MN} \cdot \mathrm{m}^{-1/2}$ $0.53 \pm 0.09 \, \mathrm{MN} \cdot \mathrm{m}^{-1/2}$
Tensile strength	$\sigma_{\mathrm{t}1}$ $\sigma_{\mathrm{t}2}, \sigma_{\mathrm{t}3}$	$1.2 \cdot 10^6 \, \mathrm{Pa}$ $0.6 \cdot 10^6 \, \mathrm{Pa}$
Isotropic equivalents		
Intrinsic permeability	K	$0.8 \cdot 10^{-19} \, \mathrm{m}^2$
Elastic modulus	E	$11.2 \cdot 10^9 \, \mathrm{Pa}$
Poisson's ratio	ν	0.37
Shear modulus	G	$4.09 \cdot 10^9 \, \mathrm{Pa}$
Fracture toughness	K_I	$0.39 \, \mathrm{MN} \cdot \mathrm{m}^{-1/2}$
Tensile strength	σ_t	$0.8 \cdot 10^6 \, \mathrm{Pa}$

3.1.1. *Determination of fracture parameters*

To apply the presented framework, we propose a deduction of the fracture parameters from the material properties listed in **Table 1**. Using the isotropic equivalent properties, we compute the experimental fracture energy $\mathcal{G}$ (**Eq. 28**) with $E' = \frac{E}{1-\nu^2}$ for plane strain or else $E' = E$ as given by linear elastic fracture mechanics. The characteristic length ℓ_ch is given by **Equation 29**.

$$\mathcal{G} = \frac{K_\mathrm{I}^2}{E'} \tag{28}$$

$$\ell_\mathrm{ch} = \frac{K_\mathrm{I}^2}{\sigma_t^2} = \frac{\mathcal{G}E'}{\sigma_t^2} \tag{29}$$

The length scale ℓ (**Eq. 24**) needs to be calculated as follows (65) (**Eq. 30**).

$$\text{AT}_1 : \ell = \frac{3}{8}\ell_{\text{ch}} \qquad \& \qquad \text{AT}_2 : \ell = \frac{27}{256}\ell_{\text{ch}} \tag{30}$$

Finally, the fracture energy used in the simulation $\mathcal{G}_{\text{c,sim}}$ is calculated from the ratio between the mesh size h and length scale parameter ℓ (10, 76). The mesh dependency of the fracture energy is a long standing issue in damage mechanics (50). However, in phase-field models, this dependency can be quantitatively taken into account (10, 65, 76) as shown in **Equation 31**.

$$G_{\text{c,sim}} = \frac{\mathcal{G}}{\left(1 + \frac{3h}{8\ell}\right)} \tag{31}$$

The obtained values for the current material are summarized in **Table 2** for both the plane-strain and three-dimensional settings.

3.2. Model setup

We prepared a field-scale model that represents a quarter cross-section of the open niche in two dimensions. In this study, the simulations were performed in an isotropic setting because the proposed crack phase-field approach does not account for anisotropic elastic properties. For this, we used isotropic equivalent properties (**Table 1** and **Table 2**). We aim to extend the methodology using the anisotropic phase-field formulation proposed in (81). **Figure 4** shows the considered domain and setup. This represents a quarter of the niche in the radial direction. To improve the crack resolution and use further experimental data to set up the model, we reduced the mesh size according to the measured apertures in the scanline (53), which varied from $0.1 \cdot 10^{-3}$ m to $3.5 \cdot 10^{-3}$ m. For this reason, we

Table 2: Parameters related to the crack-phase-field formulation.

Parameter	Value (setting)	
	Plane-strain	3D
E'	13 GPa	11.2 GPa
l_{ch}	0.24 m	0.24
$\ell : \text{AT}_1$	0.09 m	0.09 m
$\ell : \text{AT}_2$	0.025 m	0.025 m
$\mathcal{G}$	11.7 N/m	13.6 N/m
d_{irr}	0.05	0.05

prepared a locally refined mesh with smallest element edge length between $2.0 \cdot 10^{-3}$ m and $2.5 \cdot 10^{-3}$ m. Note that an "actual" fracture typically occupies physically negligible thicknesses, which are not practical to resolve in a finite element simulation. Due to this, the "actual"/sharp fracture is smeared/diffused in approaches such as the phase-field. This does not imply that the "actual" sharp fracture is physically spread, but that it can propagate within the numerically smeared region. The numerical studies of (75) established that the crack aperture can be recovered with different mesh sizes,

Figure 4: Quarter model of the CD-A experiment **(a).** The total size of the model was 50x50m². Dirichlet boundary conditions are shown. Where not stated, homogeneous Neumann boundary conditions were applied. The blue dashed line frames the window where the results are visualized in the following sections. For completeness, meshes inside the visualization window **(b)** and near the niche wall **(c)** are shown.

and consequently, crack resolutions. The resolution of the "numerical" fracture is represented by the length scale ℓ, which is computed using **Equation 30** (**Table 2**). For example, the phase-field for AT_1 transition from 0 (intact) to 1 (crack) over 2ℓ elements and its optimal profile, which is obtained by minimizing **Equation 17** with respect to d, follows a quadratic function for uniform G_c (75). For the size of ℓ, it is recommended to be at least twice the element size h (i.e. $2h \leq \ell$) in (40, 46). Therefore, a larger ℓ implies a less resolved crack and allows a larger element size. Considering the relationship between h and ℓ, the crack resolution can be increased to $\ell = 5 \cdot 10^{-3}$ m.

Figure 5: Relative humidity (RH) drop and respective pore pressure evolution within time.
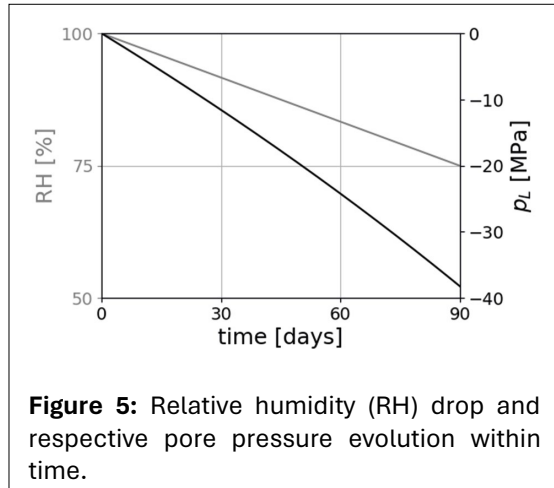
The fracture energy $G_c = 11.7$ N/m was calibrated according to h and ℓ for the plane strain conditions and AT_1 formulation (**Eq. 31**). The obtained mesh contains 52,576 quadrilateral elements (Taylor-Hood for $\mathbf{u} - p_L$ and linear elements for the crack phase-field). We set the time step size to 1 day (86,400 s) for the first two weeks of the simulation, where no cracks nucleate, and to 600 s for the remaining time, because we needed a finer temporal discretization to aid in the convergence of the crack phase-field evolution.

To model the drying behavior, the liquid pressure development computed from the measured relative air humidity (**Fig. 2**) with the Kelvin equation (66) (**Equation 32**) was applied at the wall of the niche.

$$p_L = \frac{\rho_L RT}{M_L} \ln(\text{RH}) \tag{32}$$

While $T = 288$ K stands for the constant ambient temperature, the universal gas constant and molar mass of the pore fluid are given by $R = 8.314$ J / (mol K) and $M_L = 0.01802$ kg / mol, respectively. The determination of the pressure boundary condition at the niche wall is based on the in-situ observed drop in RH from a fully saturated state (RH = 100%) to the lowest monitored value (RH = 75%) in the first winter (**Fig. 2**). **Figure 5** shows the computed/applied pressure boundary condition. The remaining boundaries were modelled as impermeable. Symmetry boundary conditions were applied to the domain and are shown directly in **Figure 4**. Furthermore, it is important to emphasize that we did not impose initial cracks in the model.

Table 3: Minimum and maximum values of each strain component after 15, 21, and 30 days of drying. The reported values correspond to individual scales for each of the visualizations shown in **Figures 7** and **8**, i.e. are not given of a particular element. A threshold filter is applied on the crack field, e.g. elements with $d \geq 99$% are blended out, to determine the minima and maxima of the strain components, otherwise the degraded strain/stress fields would lead to drastic/unrealistic strain component values.

Strain component	15 days [10^{-4}]		21 days [10^{-4}]		30 days [10^{-4}]	
	Min	**Max**	**Min**	**Max**	**Min**	**Max**
ε^{hyd}	-1.50	0.05	-2.30	0.20	-2.80	0.39
ε_x^{dev}	-1.49	1.49	-1.87	1.03	-1.98	1.03
ε_y^{dev}	-1.49	1.49	-1.03	1.87	-1.03	1.98
ε_{xy}^{dev}	-1.49	0.26	-1.65	0.48	-1.65	1.39

3.3.   Hydro-mechanical effects

The full framework is solved according to the steps defined in Section 2.4 for the homogeneous setup as described in Section 3.2. To provide a detailed discussion on the model response, its hydro-mechanical effects and cracking are discussed separately.
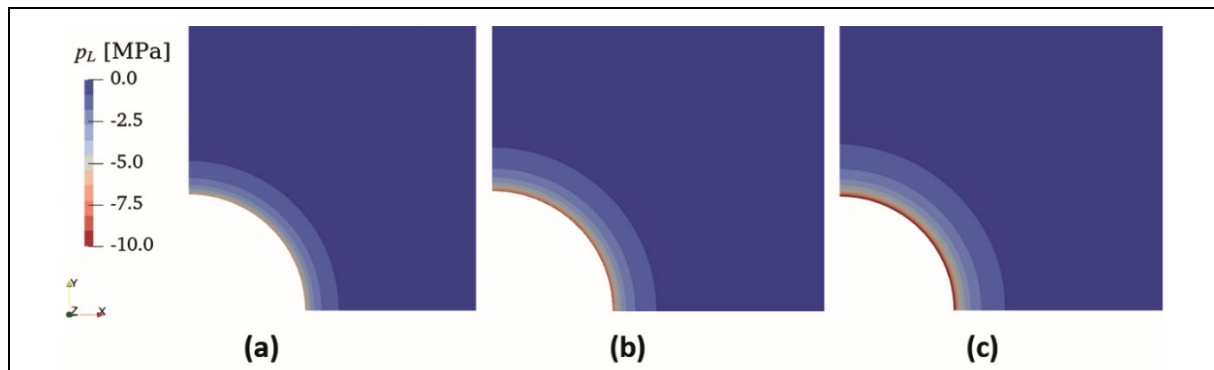
Figure 6: Liquid pore pressure evolution after **(a)** 15, **(b)** 21, and **(c)** 30 days of drying. The largest suction is found at the niche wall, where the drying boundary condition was applied. It decreased with increasing distance from the niche wall. The desaturated zone increased with time (see **Fig. 11** for comparison).
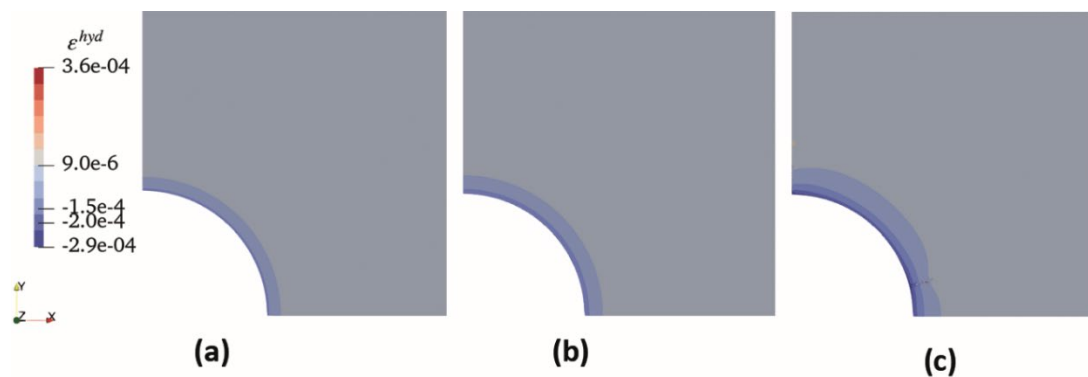
Figure 7: Hydrostatic strains after **(a)** 15, **(b)** 21, and **(c)** 30 days of drying. Up to cracking, the strains increased uniformly within the domain. The maximum value was chosen to facilitate the comparison with **Figure 8**.
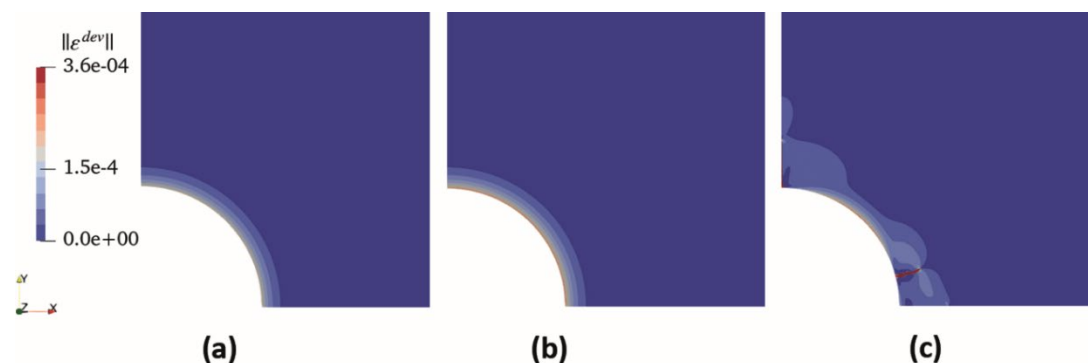
Figure 8: Norm of deviatoric strains after **(a)** 15, **(b)** 21, and **(c)** 30 days of drying. Up to cracking, the strains increased uniformly within the domain. As the norm is depicted, all the values are in the positive range. **Table 3** provides a detailed overview on the deviatoric strain increase.

The rock desaturates due to drying from the niche wall. Large suctions (lowest liquid pressures, and consequently lowest saturations) were achieved at the niche wall. We further characterized and interpreted the water content changes in the vicinity of the niches using numerical modeling and in-situ measurements (18, 83, 84). The pore pressure evolution after 15, 21, and 30 days of drying is shown in **Figure 6**. Note that the desaturated zone increases with time up to 0.22 m (see **Fig. 11** where the saturation is shown, for completeness).

During drying, the pore pressure was the main driving load. As the no swelling model was considered, the mechanism is reversible, i.e. pressure changes cause effective stress changes which result in strains. The evolution of the hydrostatic $\varepsilon^{\mathrm{hyd}}$ and Frobenius norm of the deviatoric strain $\|\varepsilon^{\mathrm{dev}}\|$ are plotted in
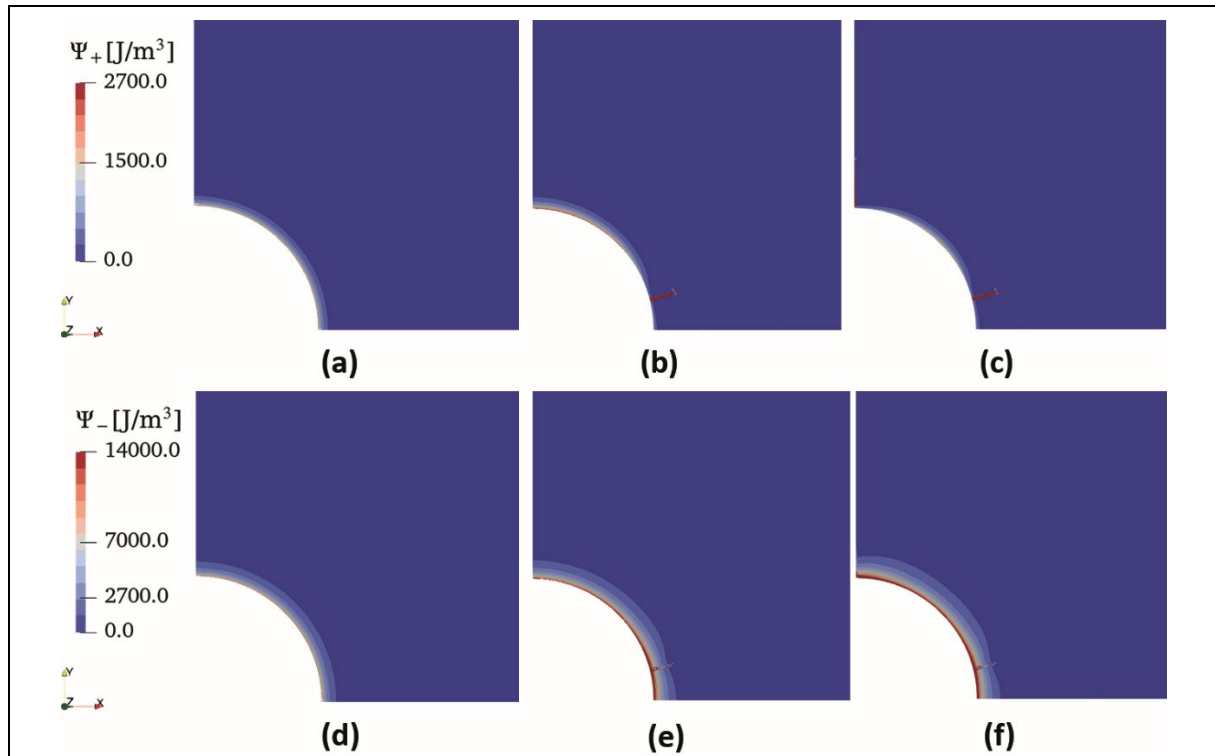
Figure 9: Strain energy response after **(a, d)** 21, **(b, e)** 28.5, and **(c, f)** 30 days of drying. The active **(a-c)** Ψ+ and **(d-f)** non-active Ψ− parts of the strain energy are shown.
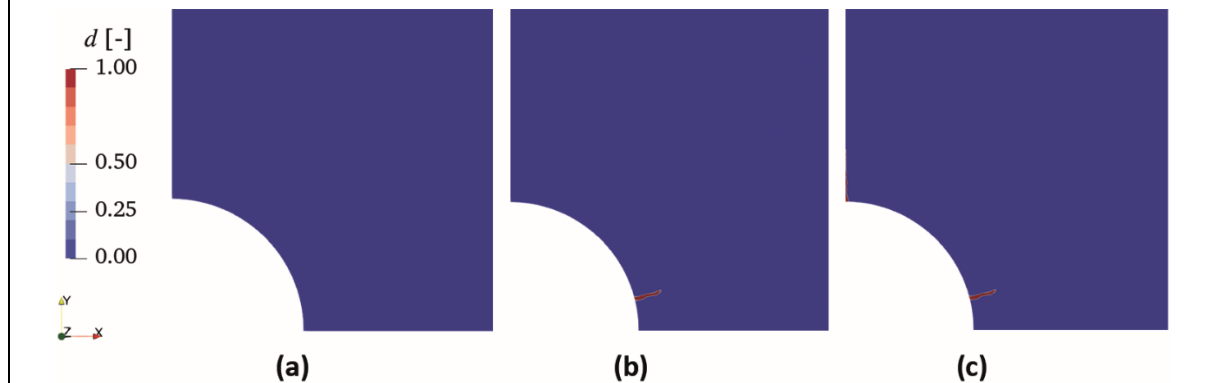
Figure 10: Phase-field evolution at **(a)** 21, **(b)** 28.5, and **(c)** 30 days of drying. While the blue color represents intact regions (d = 0), the red color depicts fully damaged (d = 1). In the visualizations to follow, the elements with at least 99% damage were blended out.
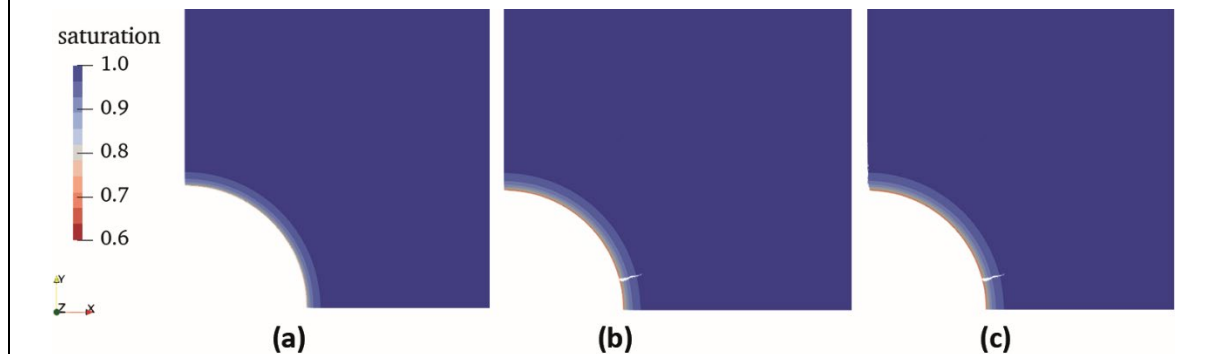
Figure 11: Degree of saturation and crack evolution at **(a)** 21, **(b)** 28.5, and **(c)** 30 days of drying. The niche wall was drier than the surrounding rock. Elements with at least 99% damage were blended out in the visualization.

Figure 7 and **Figure 8**. Before 21 days, the strains increased uniformly within the domain and no cracks initiated. The hydrostatic strains were predominantly negative, corresponding to shrinkage.

The minimum and maximum values of each component are reported in **Table 3**. In particular, the values prior to cracking, i.e. before the strain/stress field is degraded, are relevant. When the elements are fully damaged, there is a drastic/unrealistic increase in the strain/stress due to the degradation function (**Eq. 21**). For this reason, we report the minima and maxima without considering damaged elements. For this reason, we expect $\boldsymbol{\varepsilon}^{\text{dev}}$ to have a stronger contribution to the active energy in comparison to the contribution from $\boldsymbol{\varepsilon}^{\text{hyd}}$ when using the volumetric-deviatoric split. This implies that the deviatoric part drives crack development. The drying of the wall leads to contraction (shrinkage) of the niche and convergence of the wall towards the center. Because the largest strains are found at the walls of the niches, we expect cracks to nucleate from this drier region. Note that the strain distributions were non-uniform after 21 days of drying (**Fig. 7b**, **Fig. 8b**), indicating crack nucleation/propagation (localization of the crack phase field). More details on the crack nucleation and consequent loss of uniformity in the, e.g. strain field, are discussed in the next section. In the following, we discuss these results in detail together with the strain energy and crack response of different test cases, as well as the impact of the chosen material parameters (**Fig. 9, Fig. 11**). Furthermore, we propose a calibration method and investigate the influence of homogeneous and heterogeneous distributions of the material properties.

3.4. Strain energy increase and crack response

The drying boundary condition leads – up to cracking – to a uniform increase of the elastic strain energy and, consequently, to a uniform increase of the damage evolution. With the phase-field modeling approach, crack initiation positions do not have to be prescribed in the mesh, and no discontinuities are explicitly added to the model. The damage/crack phase-field localization (crack initiation) starts when the uniform damage solution becomes unstable. That is, the uniform damage is no longer the local minimum of the total energy (51), i.e. the homogeneous damage solution no longer satisfies the stability condition, and a solution bifurcates to localized damage. In other words, the energy state with damage localization becomes more stable than that of a uniform damage. As a result of the damage localization (initiated crack), strain/stress fields become non-uniform. The instability related to the homogeneous damage evolution and the damage localization have been demonstrated in closed form for simpler settings in (39, 51, 59). This model feature is advantageous when dealing with desiccation cracks as we do not require ad hoc criteria or random inhomogeneities in the model. However, in a homogeneous setting, the crack localization location can be non-unique if local minima exist in the system. In addition, a symmetric evolution of the fracture propagation could also become unstable and lose symmetry (see [23, 64] for closed-form analyses under such conditions).

The increase of capillary pressure/suction (decrease of liquid pressure) contracts the rock. To understand how the strain energy evolves and consequently induces cracking, we plotted both the non-active Ψ_- and active parts Ψ_+ of the strain energy for the volumetric-deviatoric split (2) with AT_1 formulation (see **Appendix A,** available to download online, for details) in **Figure 9**. Before choosing this formulation as a basis for this work, we performed numerical tests at the laboratory scale based on the setup presented in (17), where desiccation was simulated in a clay slab that showed a similar drying/deformation mechanism as the field-scale test. The numerical tests have shown more brittle (abrupt) and deeper cracks when the volumetric-deviatoric split was applied with AT_1 formulation. Because sharper and deeper cracks are more critical for radioactive waste disposal – deeper cracks would mean a longer path for contaminant transport – we chose to use the volumetric-deviatoric split with AT_1 for more conservative analyses in this paper. Both the active and non-active parts increase uniformly prior to crack propagation. At 21 days, $p_{\text{L}} = -9.3$ MPa (RH $\approx 93\%$), max $\Psi_+ = 1{,}766.5\,\text{J/m}^3$ and max $\Psi_- = 10{,}138.9\,\text{J/m}^3$, **Figure 9,** parts **a** and **d**. Although Ψ_- is much larger than Ψ_+, the former will not affect crack development. The material would degrade uniformly if no energy decomposition was applied because, in this case, the total strain energy would govern the system without differentiating between active and non-active contributions (compare non-split and volumetric deviatoric formulations in **Appendix A**, available to download online). The increase of Ψ_- is related to compression, which is negative volume strains (**Fig. 7**). Since the positive part of $\boldsymbol{\varepsilon}^{\text{hyd}}$ is small in comparison to its negative

counterpart, the increase of Ψ_+ is predominantly governed by the deviatoric strains. The first crack nucleates after 28 days of drying (RH $\approx$ 92%). Right before nucleation max $\Psi_+ \approx 2{,}650\,\text{J/m}^3$ and max $\Psi_- \approx 15{,}000\,\text{J/m}^3$ at the niche wall (**Fig. 9 b,e**).

Figure 12: Crack location, depth, and RH along niche radius. Between 2 and 3 cracks formed in each realization. The order of their nucleation and depth of propagation are annotated at the respective RH at nucleation (vertical axis). Most cracks nucleated between 90 and 95% RH. Note that the deeper cracks localized in the random case with increased permeability.
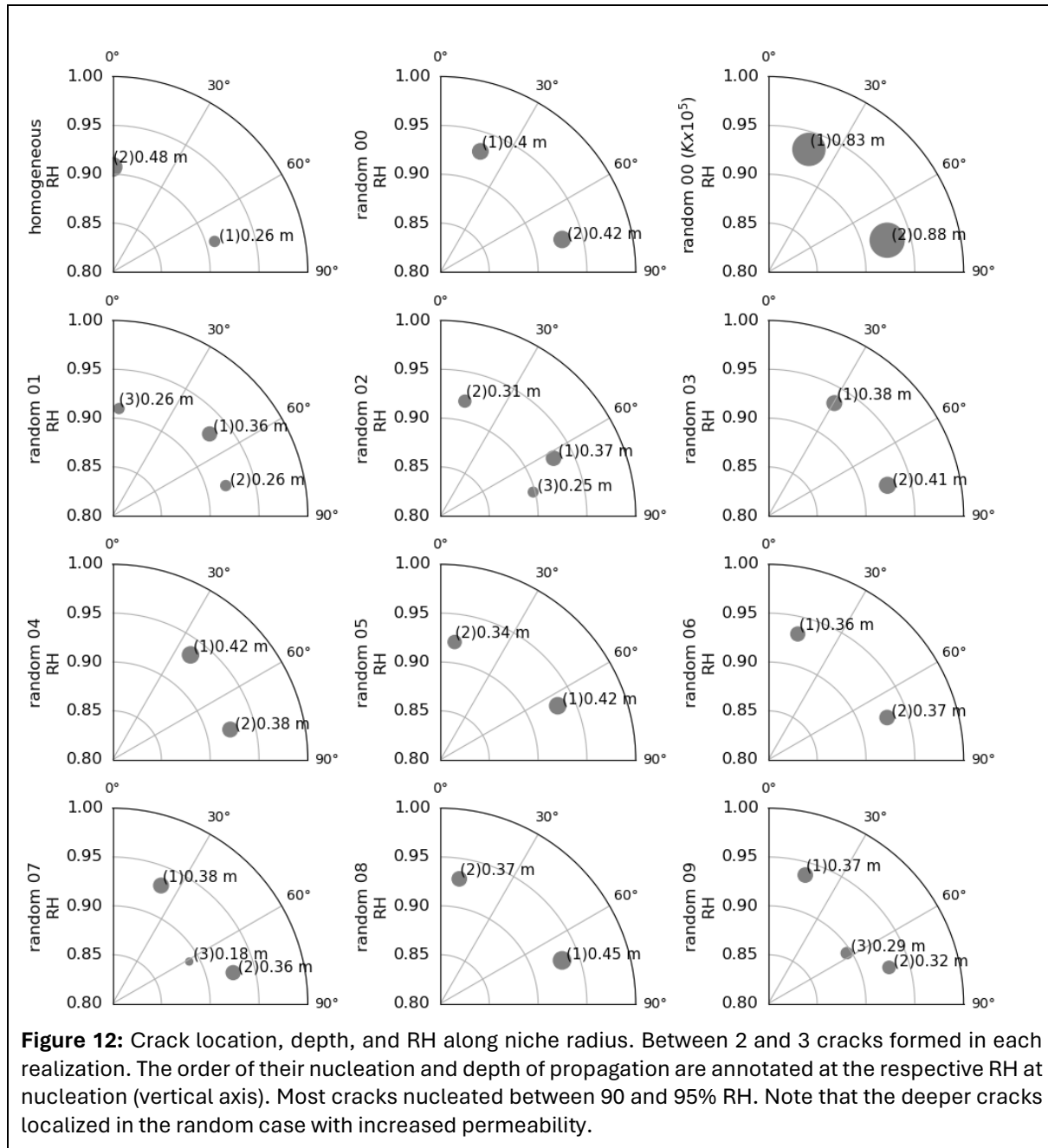
After the first crack nucleates, the energy fields become non-uniform: Ψ_+ increases near the crack tip and near the roof of the niche (upper side edge of the contour). The increase of Ψ_+ suggests further crack development in this region. Due to the increase of negative strains, Ψ_- becomes larger at the wall near the nucleation in comparison to other parts of the wall while Ψ_+ relaxes near the traction-free crack walls. With continuous increase of energy due to drying, a second crack propagates right after the first (29 days, 91.9% RH) at the roof of the niche. The active energy increases by approximately $100 - 300\,\text{J/m}^3$ with respect to the previous maximum at the onset of the new crack. This leads to further changes in the energy fields and suggests the location of the next crack, approximately in the middle of the niche. Similar non-uniformity near the cracks is also observed in the evolution of the strains in **Figure 7b, c** and **Figure 8b, c**. The third crack propagates at 89.7% RH (37.5 days). The maximum active energy increases by approximately $100 - 300\,\text{J/m}^3$ with respect to the previous maximum. The active energy does not exceed the maximum value prior to cracking. No further cracks develop up to 60 days.

Figure 10 and **Figure 11** show the crack phase-field and the liquid saturation changes, respectively. In the latter, we applied a threshold filter on the crack phase-field variable so that the elements with damage values equal to or greater than 99% were blended out for direct visualization.

Due to the refined mesh and the AT_1-formulation, the localized cracks do not show large diffusive zone in comparison to those expected with an AT_2-formulation. For this reason and to reduce the number of figures, the crack phase-field d results are depicted with the threshold filter, together with the saturation results (**Fig. 11**). The current model does not account for changes in retention behavior in the cracks which could accelerate local drainage, and it does not impose hydraulic boundary conditions on the crack faces. Therefore, any hydraulic effects due to cracking come from the hydro-mechanical coupling only. The locations of the propagated cracks along the wall angles, order of, and RH during nucleation are shown in **Figure 12**. The smallest crack propagates up to 0.24 m while the longest reaches 0.47 m. We compute further test cases in the following section and compare their nucleation conditions and crack depths, for example, RH at propagation, and number of cracks (**Fig. 12**).

This framework has also been applied in three-dimensional setting (15). In this test case, we demonstrate the influence of a mechanical wall restraint on the cracking pattern, motivated by uncertain boundary conditions in the in-situ setting. We observed a more intricate crack pattern when wall movements were hindered. This constitutes an additional mechanical effect on the drying and shrinkage process. As expected, the mechanical effect induces earlier crack propagation between 93-94% RH (suction 8-9 MPa) in comparison to the reference case in this study. The RH range was within the expected range (**Fig. 2a**). Note, however, that neither the fracture properties nor the formal steps for quantification and comparison of the patterns with monitored data are considered in the three-dimensional setup. This needs to be studied and refined further and combined with an anisotropic constitutive model to reproduce the crack orientation reported in the field (53). Furthermore, we plan to use a three-dimensional model to reproduce the distance between desiccation cracks monitored in the long term.

3.4.1. Random distributions and realizations

In the simulations performed up to this point, the values from **Tables 1** and **2** were used directly as the input parameters in the model. The obtained parameters consist of "best estimates", for example, those determined from a weighted average of the measurements from several experiments (7). Parameters such as the intrinsic permeability and fracture energy have a strong influence on the desiccation process, as shown in (14, 17). Porosity is also an important parameter when dealing with porous media because it influences the water availability in the material, as discussed in (14). In the following simulations, random-field parameterizations were used for these properties. For this purpose, the parameter values were assigned in an element-wise
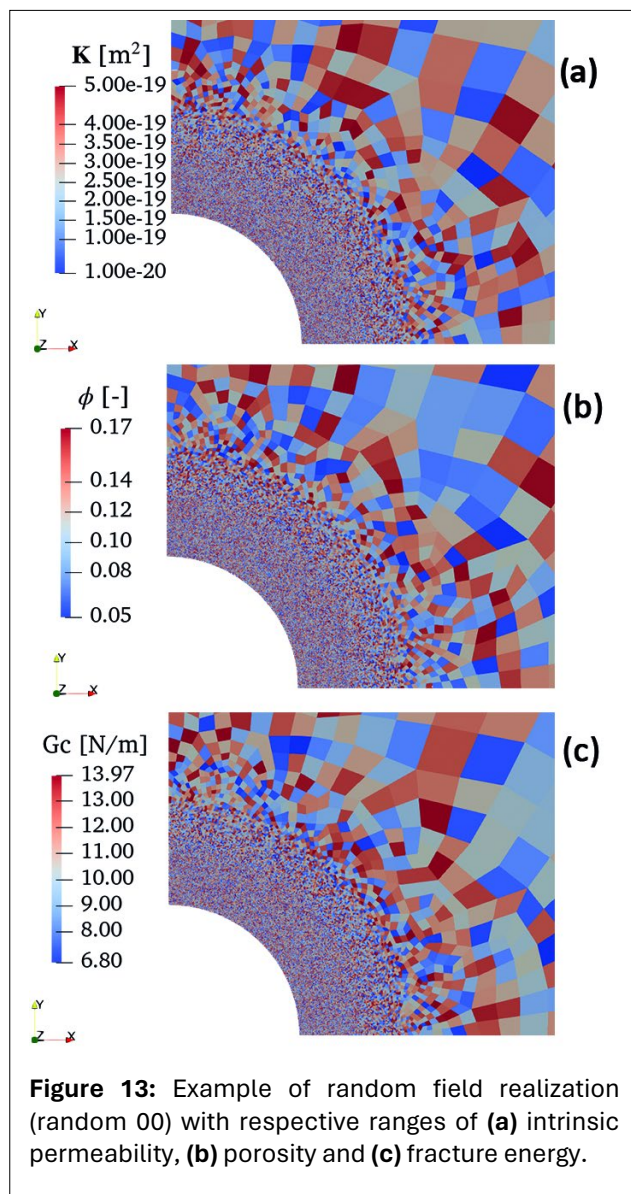
Figure 13: Example of random field realization (random 00) with respective ranges of **(a)** intrinsic permeability, **(b)** porosity and **(c)** fracture energy.

manner based on a uniform random distribution within the measurement ranges of K and n, while the G_c values were estimated from the K_I and E' ranges (**Fig. 13**). The present study focuses on identifying the leading parameters for crack initiation. Therefore, we do not consider more elaborate techniques for applying and computing random fields. The mesh was refined in the locations where cracks were expected to initiate and propagate (see Section 3.2 for details on the element size), that is, near the niche wall. There may be a mesh dependency of the random fields on the mesh near the outer boundaries because the mesh in this region is not refined. However, no cracks propagated in this region. However, no mesh dependency of the random fields is expected in the locally refined region. The relevance of this type of study lies in understanding whether the crack onset/propagation shows a strong variation when comparing the realizations and evaluating the robustness of the approach. Note that the same mesh was used throughout the homogeneous and random simulations; the models differed by the projected values of the aforementioned parameters at each finite element.

In the literature, the material properties of Opalinus Clay vary significantly (6, 7). This might be related to the strong heterogeneous nature of this material, as well as to the different testing conditions and methods. These aim at determining a single property or a small set of parameters and not the "full" range of material properties and their correlation. For this reason, the randomized fields are implicitly not correlated, and the lower and upper ranges of each property obtained from the literature are projected:

$$0.05 \leq \phi \leq 0.175$$

$$0.08 \cdot 10^{-19} \, \text{m}^2 \leq K \leq 4 \cdot 10^{-19} \, \text{m}^2$$

$$6.80 \, \text{N/m} \leq G_c \leq 13.96 \, \text{N/m}$$

We simulated 10 realizations, i.e. calculations with different random property distributions, using the volumetric-deviatoric split and AT_1 formulation.

For completeness, we compared the hydraulic response with the homogeneous case and observed that the extent of the desaturated zone is larger and more distributed as shown in **Figure 14** (**Fig. 6** for comparison). This might be a result of the random distribution of the permeability, which allows the drying front to be distributed further along the model.

Figure 15 shows the first realization. The locations of the cracks from this and further realizations are shown in **Figure 12**. Note that in this case, only two desiccation cracks develop. These cracks were approximately 0.4 m deep and nucleated after 21 days of drying, earlier than in the homogeneous reference case. To investigate the reason for the earlier propagation, we checked the values of the random properties at the locations where cracks nucleated. In the center of the first crack, $K = 3.6 \cdot 10^{-19} \, \text{m}^2, \phi = 0.05$ and $G_c = 10.05$ N/m, while in the second crack $K = 0.35 \cdot 10^{-19} \, \text{m}^2$, $\phi = 0.15$ and $G_c = 7.49$ N/m. In both cases, G_c was smaller than the "best estimate", which contributes to earlier crack propagation. This fact might be enhanced by the lower ϕ in the first crack, i.e. less water availability, and the lower K in the second crack, i.e. delayed drainage. Moreover, the desaturation of the neighbor elements affects the local strains and hence cracking potential, contributing to a more diffuse/indirect effect of K. In other realizations, a decreased fracture energy was registered in the crack nucleation points. The results of all realizations are summarized in **Figure 12**.

3.4.2. *Crack propagation and increase of permeability*

As depicted in the plots of the saturation and crack localization, the nucleated cracks do not affect the saturation changes directly. This is due to the weak coupling between the pore pressure and crack fields of the current framework, i.e. crack development does not change the permeability. However, previous studies have shown that the presence of cracks might increase the permeability of the porous medium and that cracks (heterogeneities) are drier in comparison to an intact surrounding, e.g. niche wall (84).
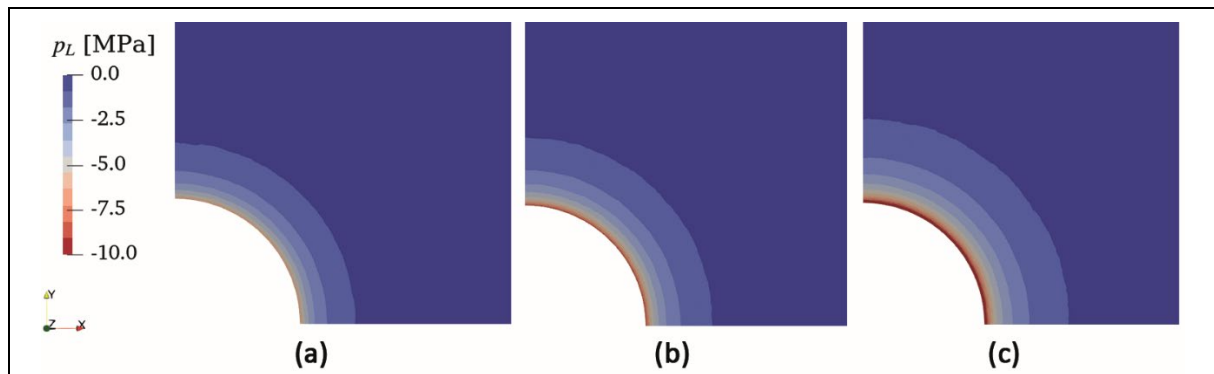
Figure 14: Liquid pore pressure evolution after **(a)** 15, **(b)** 21, and **(c)** 30 days of drying in the random test case (realization 00 for comparison with homogeneous test case). The largest suction was found in the niche wall, where the drying boundary condition was applied. The desaturated zone increased with time and was larger than the homogeneous variant.
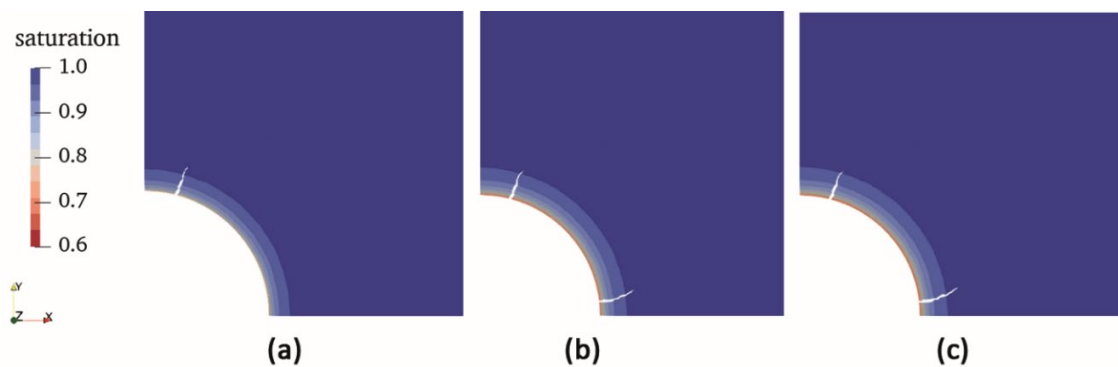
Figure 15: Degree of saturation and crack evolution at **(a)** 21, **(b)** 28.5, and **(c)** 30 days of drying in the random test case (random 00 realization). The niche wall was drier than the surrounding rock. Elements with at least 99% damage were blended out in the visualization.
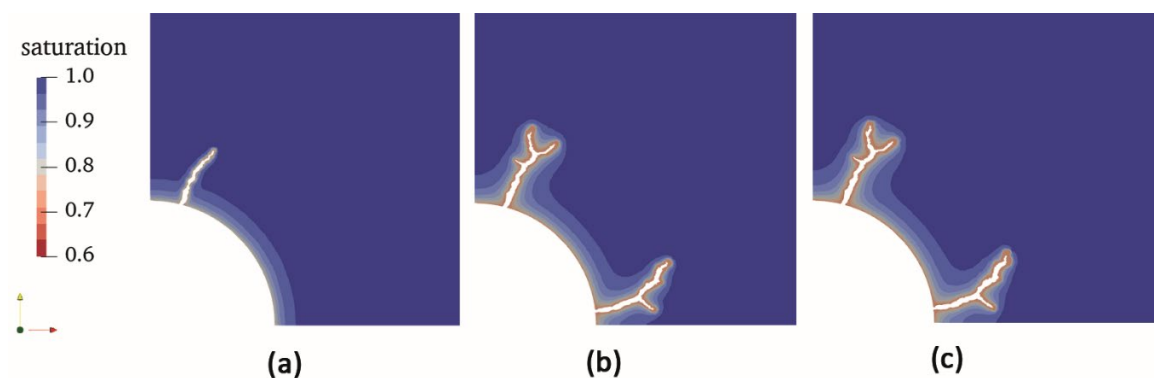
Figure 16: Degree of saturation and crack evolution at **(a)** 21, **(b)** 28.5, and **(c)** 30 days of drying in the random test case with increased permeability. The niche wall was drier than the surrounding rock. Elements with at least 99% damage were blended out in the visualization. Note that the cracks are deeper than the random 00 case and branch due to the additional "drying load" from the locally increased permeability.

To analyze the effect of increased permeability, we assigned increased permeability to the crack once it nucleated, i.e. $K \cdot 10^5$, where the material was at least 99% damaged. Note that the main idea of the test is to evaluate the influence of a sudden increase in permeability in the vicinity of the initiated crack on its propagation. For this reason, no elaborate laws/regimes have been "imposed" to induce a progressive permeability increase, e.g. (56, 77), but a limited number of cases have been studied. **Figure 16** shows the results using the field parameterization and mesh of the first realization (see **Fig. 15** – random 00 – for comparison). Because crack nucleation triggers a permeability change prior to the first cracking, the model response is similar, i.e. one nucleation. Once the crack was initiated, its propagation was much

faster than that of the previous random 00 model. The saturation field was affected by faster drainage through the cracks, leading to further drying around the cracks. This dryout owing to accelerated drainage can be interpreted as an additional drying surface (layers). This has been confirmed in experimental tests with intact and cracked samples composed of cement-based materials using neutron radiography to trace liquid changes (14, 31). Owing to this additional local load, the evolved drier cracks could propagate further. In the calculated example, the first crack propagates 0.6 m with 0.2 m branches, while the second one is 0.8 m deep with a 0.15 m branch.

4. SUMMARY AND PRACTICAL USE OF THE FRAMEWORK

The proposed unsaturated hydro-mechanical framework combined with the phase-field approach for brittle fracture was applied to simulate in-situ desiccation cracks in Opalinus Clay. The material properties were collected and simplified for the isotropic cases. The experimental data related to the aperture were used to improve the numerical crack resolution. In the following, we summarize the main results of this contribution as well as practical information for applying the framework.

4.1. Summary

We compared the response of the volumetric-deviatoric decomposition split with the AT_1 formulation. The unsaturated hydro-mechanical model with the phase-field approach was applied, and we first evaluated the pore pressure and strain responses. Enforced by the RH reduction (desaturation) measured in the field, the pore pressure acted as a drying load to induce strain evolution. Consequently, the increased strain energy drives the crack propagation. No diffuse cracked zone was formed at the wall of the niche when using the AT_1 formulation, i.e. the cracks localized in an abrupt, brittle way in comparison to those expected if using an AT_2 formulation. In all the tested cases (reference, random, and increased permeability near the crack), the nucleated cracks evolved within the experimental range, as shown in

Figure 2. **Figure 12** shows the locations of the simulated cracks and the respective RH values at which they nucleated. Two to three cracks were formed in the wall of the niche. The majority of the cracks nucleated between 90% and 95% RH and lie within the experimentally monitored range, as depicted by the gray curve in **Figure 2b**. Similar to the simulation, the number of drying cracks, represented by the sum of apertures (black curve in **Fig. 2b**), tends to increase with decreasing RH. Other interesting aspects include the depth at which the drying cracks propagate and the distance between them (e.g. crack frequency and orientation). The latter may be reproducible when setting a three-dimensional anisotropic setup with the deduced fracture properties suggested in this study. However, the feasibility and potential benefits associated with more complex models must be balanced. A direct overview of the number of cracks, their RH at nucleation, and their depth is shown in **Figure 17**.

Figure 17: The majority of cracks have initiated at relatively large RH **(a)** and have propagated up to 0.35 m inside the rock **(d).**
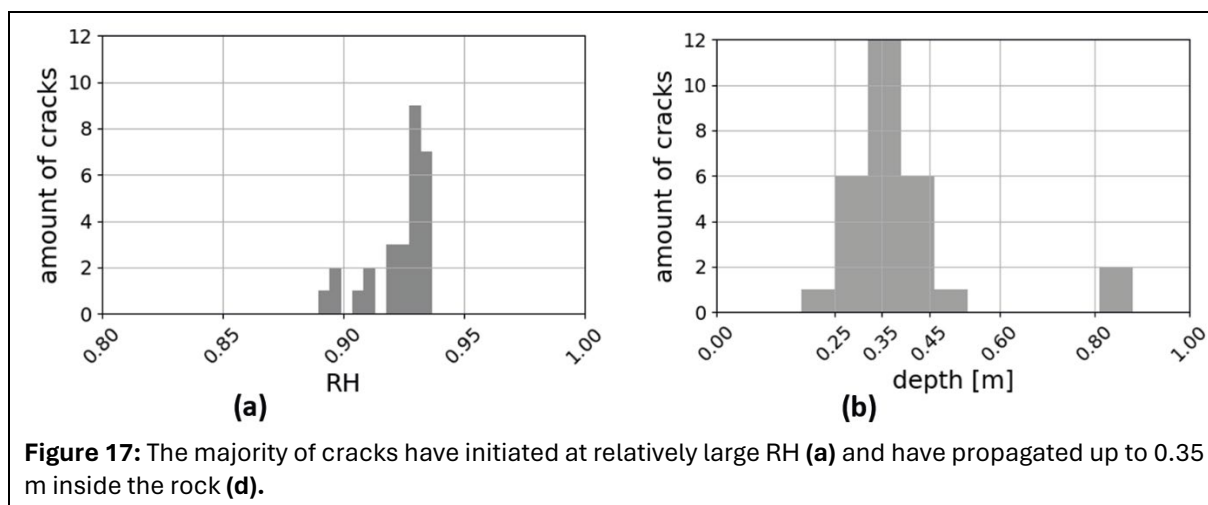
Most of the cracks propagated 0.35 m into the rock. Regular measurements of the electrical resistivity around the open niche wall have been carried out and zones with resistivity values larger than those measured initially have been identified. These zones have a corresponding lower saturation and are

located near the niche wall (maximum of 0.3 m distance from the wall into the depth of the rock) (18). This might indicate open drying cracks that, consequently, do not propagate deep into the rock (84). In-situ geological characterization is necessary to further investigate these locations and their causes.

The number of cracks and the RH range in which they nucleated were not strongly affected by different realizations with homogeneous and random properties. This demonstrates the robustness of the framework with respect to the crack response. The fracture energy, influenced by the ranges of the elastic modulus, Poisson's ratio, and tensile strength, has a strong influence on crack nucleation. In test cases with random properties, cracks were prone to occur earlier in regions with lower fracture energies.

The larger permeability and porosity induce drier regions that enhance crack propagation. To understand the effect of hydraulic property changes in cracked regions, we performed a test with a permeability function that increased when the material was damaged by at least 99%. The increased permeability in the cracks led to drier regions, which constituted an additional mechanism for further crack propagation and branching. Adding the increased permeability in a local manner, i.e. once the crack propagates and, in its vicinity, does not lead to additional crack propagation from the niche wall. Furthermore, artificial effects such as an overall permeability increase on the wall were avoided.

4.2.   Practical use of the framework

The framework can be applied to different porous materials and implemented using OpenGeoSys software (5). The implementation was based on the mass balance and evolution equations of $\mathbf{u} - p_\mathrm{L} - d$ (**Eqs. 8**, **9** and **26**). The effective stress concept (**Eq. 13**), and capillary pressure (**Eq. 3**), computed from the phase pressures (**Eq. 1**) were used to describe the behavior of the macroscopic porous media. The saturation (**Eq. 4-5**), relative permeability (**Eq. 6**), and elastic properties (**Appendix A**, available to download online) were computed at the constitutive level. Note that the evolution of d further degrades (**Eq. 22**) the effective stress (**Eq. 23**) and that the degradation acts on the active part of the strain energy (**Appendix A**, available to download online).

In this study, a framework was used to simulate drying of Opalinus Clay. First, the material properties listed in Table 1 were determined. Subsequently, we calculated the experimental fracture energy (**Eq. 30**), and the characteristic length (**Eq. 31**). Finally, we determined the maximum allowed length scales for the AT_1 and AT_2 formulations (**Eq. 32**). The proposed parametrization does not require fitting and is performed in a systematic and deductive manner. We simplified the in-situ setup and prepared a model in which the element size was locally refined to at least half of the crack resolution ($h \leq \ell/2$). If additional experimental information on the crack aperture is available, it can be used to determine the mesh size that correlates with the computed crack opening aperture. The fracture energy for the input in the simulation was computed for the chosen discretization and length scale using **Equation 33**. The model setup was complemented with the boundary conditions obtained from the experiment, e.g. the drying pore pressure computed from monitored relative humidity data.

5. CONCLUSIONS AND FUTURE RESEARCH

The main conclusions and contributions of this research are reported and correlated with future research in the following areas.

5.1.   Crack initiation and propagation

The applied unsaturated hydro-mechanical model with a phase-field approach was able to numerically reproduce desiccation crack initiation and propagation within the experimentally monitored RH range of the in situ CD-A experiment. One important point of this contribution is the deduction of the fracture parameters such as the fracture energy G_c and length scale ℓ. These two quantities affect the tensile strength of the material and, consequently, crack initiation. Further studies with combined pairs of mesh element sizes and length scales will be considered.

5.2. Experimental correlation

The computed length scale ℓ was interpreted as minimum crack resolution for the mesh. It has been linked with the experimentally monitored aperture during desiccation of the niche and used as input in the model. The modeled cracks were initiated in the same RH range as that monitored during the in-situ experiment. The simplified nature of the model, for example, isotropic and two-dimensional, allowed us to use and compare experimental data, such as the crack aperture and RH range. This is an important step towards quantitative comparison and might be sufficient for evaluating the number of cracks and their corresponding ranges. Further correlation with experimental data, such as the distance between the cracks along the niche, their frequency, length, and sum of apertures, requires a three-dimensional model with the formal deduction of fracture properties proposed in this work. Furthermore, we plan to use further long-term measurements carried out in the CD-A niches because they provide a way to validate the modeled desaturated zone and correlate it with cracking.

5.3. Material models

Another ongoing, important study is the consideration of mechanical and hydraulic anisotropy. We expect to be able to obtain desiccation cracks parallel to the bedding direction – the direction in which they propagate in the field ([53]) – once anisotropy is taken into account in the mechanical, hydraulic, and fracture behaviors. We aim to extend the methodology by using the anisotropic constitutive models proposed in ([81]). As the currently used isotropic constitutive model is prone to cracking within the expected experimental RH range, the feasibility and potential benefits associated with more complex material models and setups need to be investigated and balanced.

5.4. Local effects

The local effect of an increase in permeability in the cracked region has been studied and has impacted the depth of the propagated crack. A stricter determination of the flow regime in the vicinity of the crack is required to determine whether and how permeability changes during cracking. We plan to combine monitored water content data and geological observations, such as lithology type and heterogeneities, with modeled crack evolution.

5.5. Coupling and cyclic behavior

Another important aspect is to consider the swelling properties of clay ([61]) and evaluate their effects on the strain and strain energy responses. The seasonal behavior reported in the CD-A experiment motivated the extension of the current method to account for cyclic drying-wetting paths and their effect on cracking, for example, primary and further drying-wetting retention paths and the correlation with crack opening-closing. Further interesting studies are related to the coupling, e.g. temperature, degradation function and formulation, e.g. combination of different energy splits with AT_1 and AT_2, as well as the use of adaptive mesh refinement techniques. Finally, cracks due to excavation could lead to an initial damaged field near the excavated zone, which can be interpreted as the initial boundary condition for the crack phase field, and might influence localization and further crack propagation during drying/desiccation.

5.6. Random fields

A secondary study involved the application of random fields to the mesh. These have had less influence on the number of cracks and their propagation and have confirmed the robustness of the framework. An interesting study would be to consider different types of random fields and mesh sizes, as well as different pairs of mesh sizes and length scales, so that further effects on crack initiation might be stated.

5.7. Model abstraction

The information obtained from "detailed" models – like the one proposed in this paper – can be used to improve process understanding related to radioactive waste disposal, e.g. how do cracks form in excavated regions when these are open for ventilation/operation? What are the critical conditions for this phenomenon? How deep do these cracks propagate and influence the containment providing rock zone? Such studies might support strategies for simplification and lead to more abstract/less detailed models that are relevant to large spatial and temporal scales of safety and performance assessment. Our

examples show the first results on the mechanism behind the evolution of desiccation cracks at the field scale, under which RH conditions might develop, and how deep they can propagate within the rock (Summary).

STATEMENTS AND DECLARATIONS

Supplementary Material

See **Appendix A** for information on the "Strain Energy Decomposition", which can be found online with this paper here.

Acknowledgements

Author Contributions

All authors reviewed the manuscript. TC and KY conceptualized the presented framework and setups. KY implemented the framework. TC. developed the methodology and performed the computations. The manuscript was written by TC with support from GZ, JM, TN, and KY. Authors GZ, JM and TN dealt with the formal analysis.

Conflicts of Interest

The authors declare that they have no known competing financial interests or personal relationships that could have appeared to influence the work reported in this paper.

Data, Code & Protocol Availability

The code and any related data and instructions used for this paper are available for download at https://gitlab.opengeosys.org/KeitaYoshioka/ogs/-/tree/RMPhF_rebase/.

Funding Received

ORCID IDs

Tuanny Cajuhi   https://orcid.org/0000-0002-0609-7291

Gesa Ziefle   https://orcid.org/0000-0002-0775-2008

Jobst Maßmann   https://orcid.org/0000-0001-9481-2816

Thomas Nagel   https://orcid.org/0000-0001-8459-4616

Keita Yoshioka   https://orcid.org/0000-0001-7518-6952

Correction from May 3, 2024:

Please note that the pdf for this article was updated on May 3, 2024. Following online publication, the authors noticed some errors regarding the use of italics and bolding in several equations.

REFERENCES

1. Ambati, M., Gerasimov, T., & De Lorenzis, L. (2015). Phase-field modeling of ductile fracture. *Computational Mechanics*, *55*(5), 1017–1040. https://doi.org/10.1007/s00466-015-1151-4

2. Amor, H., Marigo, J.-J., & Maurini, C. (2009). Regularized formulation of the variational brittle fracture with unilateral contact: Numerical experiments. *Journal of the Mechanics and Physics of Solids*, 57(8):1209 – 1229. https://doi.org/10.1016/j.jmps.2009.04.011

3. Balay, S., Abhyankar, S., Adams, M. F., et al. (2019a). PETSc Users Manual. Technical Report ANL-95/11 - Revision 3.11, Argonne National Laboratory. https://publications.anl.gov/anlpubs/2019/12/155920.pdf

4. Bilke, L., Fischer, T., Naumov, D., et al. (2022 April). OpenGeoSys, Zenodo, version 6.4.3. https://doi.org/10.5281/zenodo.7092676

5. Bilke, L., Flemisch, B., Kalbacher, T., et al. (2019). Development of open-source porous media simulators: Principles and experiences. *Transport in Porous Media*, 130(1), 337–361. https://doi.org/10.1007/s11242-019-01310-1

6. Bock, H. (2009, June 30). RA Experiment. Updated review of the rock mechanics properties of the Opalinus Clay of the Mont Terri URL based on laboratory and field testing. Unpublished Manuscript, Mont Terri Project, TR 2008-04. https://www.mont-terri.ch/en/documentation/technical-reports.detail.document.html/mont-terri-internet/en/documents/technical-reports/TR2008-04.pdf.html

7. Bossart, P., Bernier F., Birkholzer J., *et al.* (2018). Mont Terri rock laboratory, 20 years of research: introduction, site characteristics and overview of experiments. In: Bossart, P., Milnes, A. (eds) Mont Terri Rock Laboratory, 20 Years. Swiss Journal of Geosciences Supplement, vol 5. Birkhäuser, Cham. https://doi.org/10.1007/978-3-319-70458-6_1

8. Bourdin, B. (2007). Numerical implementation of the variational formulation for quasi-static brittle fracture. *Interfaces and Free Boundaries*, 411–430. https://doi.org/10.4171/IFB/171

9. Bourdin, B., Francfort, G. A., & Marigo, J.-J. (2000). Numerical experiments in revisited brittle fracture. *Journal of the Mechanics and Physics of Solids*, *48*(4), 797–826. https://doi.org/10.1016/S0022-5096(99)00028-9

10. Bourdin, B., Francfort, G. A., & Marigo, J.-J. (2008). The variational approach to fracture. *Journal of Elasticity*, *91*(1–3), 5–148. https://doi.org/10.1007/s10659-007-9107-3

11. Bourdin, B., Marigo, J.-J., Maurini, C., et al. (2014). Morphogenesis and propagation of complex cracks induced by thermal shocks. *Physical Review Letters*, 112(1):1–5. https://doi.org/10.1103/PhysRevLett.112.014301

12. Brooks, R. H., & Corey, A. T. (1964). Hydraulic properties of porous media. *Hydrology papers*, Vol. 3, Colorado State University, Fort Collins, USA. https://www.engr.colostate.edu/ce/facultystaff/yevjevich/papers/Yevjevich_n3_1964.pdf

13. Burke, S., Ortner, C., & Süli, E. (2013). An Adaptive Finite Element Approximation of a Generalized Ambrosio–Tortorelli Functional. *Mathematical Models and Methods in Applied Sciences*, 23(09):1663– 1697. https://doi.org/10.1142/S021820251350019X

14. Cajuhi, T. (2019). Fracture in porous media: phase-field modeling, simulation and experimental validation. PhD thesis[Doctoral Disserstation, Technische Universität Braunschweig]. https://leopard.tu-braunschweig.de/servlets/MCRFileNodeServlet/dbbs_derivate_00045168/Diss_Cajuhi_Tuanny.pdf

15. Cajuhi, T., Haghighat, N., Maßmann, J., et al (2023). *Hydro-Mechanical Effects and Cracking in Opalinus Clay*. In: Kolditz, O., *et al.* GeomInt—Discontinuities in Geosystems from Lab to Field Scale. SpringerBriefs in Earth System Sciences. Springer, Cham. https://doi.org/10.1007/978-3-031-26493-1_2

16. Cajuhi, T., Maßmann, J., & Ziefle, G. (2021a). Building the bridge between safety requirements and numerical modeling: an example considering crack development of Opalinus clay in laboratory and field scales. *Safety of Nuclear Waste Disposal*, 1: 165–167. https://doi.org/10.5194/sand-1-165-2021

17. Cajuhi, T., Sanavia, L., & De Lorenzis, L. (2018). Phase-field modeling of fracture in variably saturated porous media. *Computational Mechanics*, 61(3): 299-318. https://doi.org/10.1007/s00466-017-1459-3

18. Cajuhi, T., Ziefle, G., Maßmann, J., et al. (2021b). Numerical modeling of hydro-mechanical coupled effects in the cyclic deformation (CD-A) experiment: First results and comparison with observations. EGU21, the 23rd EGU General Assembly, held online 19-30 April, 2021, id.EGU21-4173. https://doi.org/10.5194/egusphere-egu21-4173

19. Ehlers, W. & Luo, C. (2018). A phase-field approach embedded in the Theory of Porous Media for the description of dynamic hydraulic fracturing, Part II: The crack-opening indicator. *Computer Methods in Applied Mechanics and Engineering*, 341: 429–442. https://doi.org/10.1016/j.cma.2018.07.006

20. Francfort, G. & Marigo, J.-J. (1998). Revisiting brittle fracture as an energy minimization problem. *Journal of the Mechanics and Physics of Solids*, 46(8): 1319–1342. https://doi.org/10.1016/S0022-5096(98)00034-9

21. Freddi, F. & Royer-Carfagni, G. (2010). Regularized variational theories of fracture: a unified approach. *Journal of the Mechanics and Physics of Solids*, 58(8): 1154–1174. https://doi.org/10.1016/j.jmps.2010.02.010

22. Fredlund, D. G. & Xing, A. (1994). Equations for the soil-water characteristic curve. *Canadian Geotechnical Journal*, 31(4): 521–532. https://doi.org/10.1139/t94-061

23. Gao, H. & Rice, J. R. (1987). Somewhat circular tensile cracks. *International Journal of Fracture*, 33(3): 155–174. https://doi.org/10.1007/BF00013168

24. Garitte, B., Nguyen, T., Barnichon, J., et al. (2017). Modelling the Mont Terri HE-D experiment for the Thermal–Hydraulic–Mechanical response of a bedded argillaceous formation to heating. *Environmental Earth Sciences*, 76(9): 345. https://doi.org/10.1007/s12665-017-6662-1

25. Gawin, D. and Schrefler, B. (1996). Thermo-hydro-mechanical analysis of partially saturated porous materials. *Engineering Computations*, 13(7): 113–143. https://doi.org/10.1108/02644409610151584

26. Grunwald, N., Lehmann, C., Maßmann, J., et al. (2022). Non- isothermal two-phase flow in deformable porous media: systematic open-source implementation and verification procedure. *Geomechanics and Geophysics for Geo-Energy and Geo-Resources*, 8(3):107. https://doi.org/10.1007/s40948-022-00394-2

27. Heider, Y. (2021). A review on phase-field modeling of hydraulic fracturing. *Engineering Fracture Mechanics*, 253: 107881. https://doi.org/10.1016/j.engfracmech.2021.107881

28. Heider, Y. & Markert, B. (2017). A phase-field modeling approach of hydraulic fracture in saturated porous media. *Mechanics Research Communications*, 80: 38–46. https://doi.org/10.1016/j.mechrescom.2016.07.002

29. Heider, Y. & Sun, W. (2020). A phase field framework for capillary-induced fracture in unsaturated porous media: Drying-induced vs. hydraulic cracking. *Computer Methods in Applied Mechanics and Engineering*, 359: 112647. https://doi.org/10.1016/j.cma.2019.112647

30. Hu, H., Braun, P., Delage, P., et al. (2021). Evaluation of anisotropic poroelastic properties and permeability of the Opalinus Clay using a single transient experiment. *Acta Geotechnica*, 16(4): 2131–2142. https://doi.org/10.1007/s11440-021-01147-3

31. Hu, Z., Cajuhi, T., Toropovs, N., et al. (2023). A neutron radiography study on the drying of cement mortars: effect of mixture composition and crack length. *Cement and Concrete Research*, 172: 107245. https://doi.org/10.1016/j.cemconres.2023.107245

32. Hun, D.-A. (2020). Fracture modeling in clay materials under hydric shrinkageModélisation de fissure dans les matériaux argileux sous retrait hydrique: numerical models, comparisons with experiments and stochastic aspects [Phd thesis]. *Materials*. Université Paris-Est. NNT: 2020PESC2054. tel-03238425. https://theses.hal.science/tel-03238425v1/file/79165_HUN_2020_archivage.pdf

33. Kafle, L., Xu W.-J., Zeng, S.-Y., et al. (2021). A numerical investigation of slope stability influenced by the combined effects of reservoir water level fluctuations and precipitation: A case study of the Bianjiazhai landslide in China. *Engineering Geology*, 297:106508. https://doi.org/10.1016/j.enggeo.2021.106508

34. Kneuker, T. & Furche, M. (2021). Capturing the structural and compositional variability of Opalinus Clay: constraints from multidisciplinary investigations of Mont Terri drill cores (Switzerland). *Environmental Earth Sciences*, 80, 421. https://doi.org/10.1007/s12665-021-09708-1

35. Kolditz, O., Bauer, S., Bilke, L., et al. (2012). OpenGeoSys: an open-source initiative for numerical simulation of thermo-hydro-mechanical/chemical (THM/C) processes in porous media. *Environmental Earth Sciences*, 67(2):589–599. https://doi.org/10.1007/s12665-012-1546-x

36. Kolditz, O., Görke, U.-J., Konietzky, H., et al. (2021). *GeomInt–Mechanical Integrity of Host Rocks*. Series: Terrestrial Environmental Sciences. Springer, 2021. ISBN 978-3-030-61908-4, DOI: 10.1007/978-3-030-61909-1.

37. Lewis, R. W., Schrefler, B. A. (1999). The Finite Element Method in the Static and Dynamic Deformation and Consolidation of Porous Media (2nd ed). John Wiley & Sons. ISBN: 978-0-471-92809-6.

38. Lorenzis, L. D. & Maurini, C. (2021). Nucleation under multi-axial loading in variational phase-field models of brittle fracture. *International Journal of Fracture*, 237: 61-81. https://doi.org/10.1007/s10704-021-00555-6

39. Luo, C., Sanavia, L., & Lorenzis, L. D. (2023). Phase-field modeling of drying-induced cracks: Choice of coupling and study of homogeneous and localized damage. *Computer Methods in Applied Mechanics and Engineering*, 410: 115962. https://doi.org/10.1016/j.cma.2023.115962

40. Mandal, T. K., Nguyen, V. P., & Wu, J.-Y. (2019). Length scale and mesh bias sensitivity of phase-field models for brittle and cohesive fracture. *Engineering Fracture Mechanics*, 217: 106532. https://doi.org/10.1016/j.engfracmech.2019.106532

41. Marschall, P. & Giger, S. (2014). Nagra technical report 14-02, geological basics - Dossier IV - Information on geomechanics; SGT Etappe 2: Vorschlag weiter zu untersuchender geologischer Standortgebiete mit zugehörigen Standortarealen für die Oberflächenanlage -- Geologische Grundlagen -- Dossier IV -- Geomechanische Unterlagen. Technical report, National Cooperative for the Disposal of Radioactive Waste (NAGRA). ISSN 1015-2636; TRN: CH1701027088320.

42. Maßmann, J., Uehara, S.-I., Rejeb, A., et al. (2009). Investigation of desaturation in an old tunnel and new galleries at an argillaceous site. *Environmental Geology*, 57(6): 1337–1345. https://doi.org/10.1007/s00254-008-1438-2

43. Maßmann, J., Ziefle, G., Costabel, S., et al. (2020). In-situ Experiment on the Influence of Humidity on the Cyclic and Long-Term Deformation Behavior (CD-A) of the Opalinus Clay at the Mont Terri Rock Laboratory,

Switzerland: Excavation of the Twin Niches, First Measurements, Simulations and Analysis. In *EGU General Assembly Conference Abstracts*, page 9314. https://presentations.copernicus.org/EGU2020/EGU2020-9314_presentation.pdf

44. Meng, W., Wanqing, S., Jiangfeng, L., et al. (2022). Phase-field modeling of cracking process in partially saturated porous media and application to rainfall-induced landslides. *Engineering Geology*, 310: 106884. https://doi.org/10.1016/j.enggeo.2022.106884

45. Mesgarnejad, A., Bourdin, B., & Khonsari, M. M. (2015). Validation simulations for the variational approach to fracture. *Computer Methods in Applied Mechanics and Engineering*, 290: 420–437. https://doi.org/10.1016/j.cma.2014.10.052

46. Miehe, C., Welschinger, F., & Hofacker, M. (2010). Thermodynamically consistent phase-field models of fracture: Variational principles and multi-field FE implementations. *International Journal for Numerical Methods in Engineering*, 83(10):1273–1311. https://doi.org/10.1002/nme.2861

47. Mumford, D. & Shah, J. (1989). Optimal approximations by piecewise smooth functions and associated variational problems. *Communications on Pure and Applied Mathematics*, 42(5): 577–685. https://doi.org/10.1002/cpa.3160420503

48. Nguyen, G. D. & Houlsby, G. T. (2007). Non-local damage modelling of concrete: a procedure for the determination of model parameters. *International Journal for Numerical and Analytical Methods in Geomechanics*, 31(7): 867–891. https://doi.org/10.1002/nag.563

49. Nikolic, M., Ibrahimbegovic, A., & Miscevic, P. (2016). Discrete element model for the analysis of fluid-saturated fractured poro-plastic medium based on sharp crack representation with embedded strong discontinuities. *Computer Methods in Applied Mechanics and Engineering*, 298: 407–427. https://doi.org/10.1016/j.cma.2015.10.009

50. [OpenGeoSys]. (2020, May 4). *MtTerri Wisdome* [Video]. YouTube. https://www.youtube.com/watch?v=I1c8E77FEz0

51. Pham, K., Amor, H., Marigo, J.-J., et al. (2011). Gradient Damage Models and Their Use to Approximate Brittle Fracture. *International Journal of Damage Mechanics*, 20(4, SI): 618–652. https://doi.org/10.1177/1056789510386852

52. Pitz, M., Kaiser, S., Grunwald, N., et al. (2023). Non-isothermal consolidation: A systematic evaluation of two implementations based on multiphase and Richards equations. *International Journal of Rock Mechanics and Mining Sciences*, 170: 105534. https://doi.org/10.1016/j.ijrmms.2023.105534

53. Regard, V., Schefer, S., Steiner, P., et al (2022). CD-A experiment: seasonal crack mapping in twin niches. Technical report, Mont Terri Technical Note 2021-63. https://extranet.mont-terri.ch/MONT_TERRI_BASIS/2_REPORTING/1_Technical_notes/Phase_26_TN2021/TN2021_63/TN2021_63.pdf

54. Richards, L. (1931). Capillary conduction of liquids through porous mediums. *Physics*, 1(5):318–333. https://doi.org/10.1063/1.1745010

55. Sanavia, L. and Schrefler, B. (2002). A finite element model for water saturated and partially saturated geomaterials: Space and time discretisation for a multiphase porous material model. *Revue Française de Génie Civil*, 6(6): 1083–1098. https://doi.org/10.1080/12795119.2002.9692733

56. Santillán, D., Juanes, R., & Cueto-Felgueroso, L. (2017). Phase field model of fluid-driven fracture in elastic media: Immersed-fracture formulation and validation with analytical solutions. *Journal of Geophysical Research: Solid Earth*, 122(4):2565–2589. https://doi.org/10.1002/2016JB013572

57. Schrefler, B. A., Simoni, L., & Markert, B. (2017). Multifield Problems. Part 2. Solids and Structures. *Encyclopedia of Computational Mechanics* Second Edition. 1–68. https://doi.org/10.1002/9781119176817.ecm2040

58. Shashank, M. & Song, X. (2019). Coupled Analysis of Desiccation Cracking in Unsaturated Soils Through a Non-Local Mathematical Formulation. *Geosciences*, 9(10): 428. https://doi.org/10.3390/geosciences9100428

59. Sicsic, P., Marigo, J.-J., & Maurini, C. (2014). Initiation of a periodic array of cracks in the thermal shock problem: a gradient damage modeling. *Journal of the Mechanics and Physics of Solids*, 63: 256–284. https://doi.org/10.1016/j.jmps.2013.09.003

60. Stirling, R., Davie, C., & Glendinning, S. (2015). Multiphase modelling of desiccation cracking in the near-surface of compacted soils. Proceedings of the *16th European Conference on Soil Mechanics and Geotechnical Engineering*. ICE Publishing: 2311–2316. https://eprints.ncl.ac.uk/225375

61. Taherdangkoo, R., Nagel, T., Tang, Anh Minh A. M., et al. (2022). Coupled Hydro-Mechanical Modeling of Swelling Processes in Clay–Sulfate Rocks. *Rock Mechanics and Rock Engineering*, 55(12): 7489-7501. 10.1007/s00603-022-03039-8. Hal-03905361. https://doi.org/10.1007/s00603-022-03039-8

62. Tang, C.-S., Wang, D.-Y., Shi, B., et al. (2016). Effect of wetting–drying cycles on profile mechanical behavior of soils with different initial conditions. *Catena*, 139: 105–116. https://doi.org/10.1016/j.catena.2015.12.015

63. Tang, C.-S., Zhu, C., Cheng, Q., et al. (2021). Desiccation cracking of soils: A review of investigation approaches, underlying mechanisms, and influencing factors. *Earth-Science Reviews*, 216: 103586. https://doi.org/10.1016/j.earscirev.2021.103586

64. Tanné, E., Bourdin, B., & Yoshioka, K. (2022). On the loss of symmetry in toughness dominated hydraulic fractures. *International Journal of Fracture*, 237(1-2):189–202. https://doi.org/10.1007/s10704-022-00623-5

65. Tanné, E., Li, T., Bourdin, B., Marigo, J.-J., and Maurini, C. (2018). Crack nucleation in variational phase-field models of brittle fracture. *Journal of Mechanical and Physics of Solids*, 110: 80–99. https://doi.org/10.1016/j.jmps.2017.09.006

66. Thomson, W. (1872). 4. On the Equilibrium of Vapour at a Curved Surface of Liquid. *Proceedings of the Royal Society of Edinburgh*, Volume 7: 63–68. https://doi.org/10.1017/S0370164600041729

67. van Dijk, N. P., Espadas-Escalante, J. J., & Isaksson, P. (2020). Strain energy density decompositions in phase-field fracture theories for orthotropy and anisotropy. *International Journal of Solids and Structures*, 196: 140–153. https://doi.org/10.1016/j.ijsolstr.2020.04.022

68. Van Genuchten, M. (1980). A Closed-Form Equation for Predicting the Hydraulic Conductivity of Unsaturated Soils. *Soil Science Society of America Journal*, 44(5): 892–898. https://doi.org/10.2136/sssaj1980.03615995004400050002x

69. Wang, H., de La Vaissière, R., Vu, M.-N., et al. (2022a). Numerical modelling and in-situ experiment for self-sealing of the induced fracture network of drift into the Callovo-Oxfordian claystone during a hydration process. *Computers and Geotechnics*, 141:1 04487. https://doi.org/10.1016/j.compgeo.2021.104487

70. Wang, H., Dong, Q., de La Vaissière, R. *et al.* Investigation of Hydro-mechanical Behaviour of Excavation Induced Damage Zone of Callovo-Oxfordian Claystone: Numerical Modeling and In-situ Experiment. *Rock Mechanics and Rock Engineering*, 55: 6079–6102. https://doi.org/10.1007/s00603-022-02938-0

71. Wild, K. & Amann, F. (2018). Experimental study of the hydro-mechanical response of Opalinus Clay - Part I: Pore pressure response and effective geomechanical properties under consideration of confinement and anisotropy. *Engineering Geology*, 237: 32–41. https://doi.org/10.1016/j.enggeo.2018.02.012

72. Wild, K. M., Walter, P., & Amann, F. (2017). The response of Opalinus Clay when exposed to cyclic relative humidity variations. *Solid Earth*, 8: 351–360. https://doi.org/10.5194/se-8-351-2017

73. Yan, H., Jivkov, A. P., & Sedighi, M. (2022). Modelling soil desiccation cracking by peridynamics. *Géotechnique*, 73(5): 388-400. https://doi.org/10.1680/jgeot.21.00032

74. Yoshioka, K. & Bourdin, B. (2016). A variational hydraulic fracturing model coupled to a reservoir simulator. *International Journal of Rock Mechanics and Mining Sciences*, 88: 137–150. https://doi.org/10.1016/j.ijrmms.2016.07.020

75. Yoshioka, K., Mollaali, M., & Kolditz, O. (2021). Variational phase-field fracture modeling with interfaces. *Computer Methods in Applied Mechanics and Engineering*, 384: 113951. https://doi.org/10.1016/j.cma.2021.113951

76. Yoshioka, K., Naumov, D., and Kolditz, O. (2020). On Crack Opening Computation in Variational Phase-Field Models for Fracture. *Computer Methods in Applied Mechanics and Engineering*, 369: 113210. https://doi.org/10.1016/j.cma.2020.113210

77. Yu, Z., Shao, J., Duveau, G., et al. (2021). Numerical modeling of deformation and damage around underground excavation by phase-field method with hydromechanical coupling. *Computers and Geotechnics*, 138: 104369. https://doi.org/10.1016/j.compgeo.2021.104369

78. Zhang, C.-L. (2017). Response of clay rock to moisture change. *Advances in Laboratory Testing and Modelling of Soils and Shales*: 155–164. https://link.springer.com/chapter/10.1007/978-3-319-52773-4_17

79. Zhang, C.-L., Komischke, M., Kröhn, M., et al (2019). Experimental study of the mechanical behaviour of the sandy facies of Opalinus Clay at Mont-Terri. LT-A programme within the Mont-Terri-Project. Technical report, Gesellschaft für Anlagen und Reaktorsicherheit (GRS) GmbH. ISBN 978-3-947685. https://inis.iaea.org/search/search.aspx?orig_q=RN:51064336

80. Zhang, J., Niu, G., Li, X., and Sun, D. (2020). Hydro-mechanical behavior of expansive soils with different dry densities over a wide suction range. *Acta Geotechnica*, 15(1): 265–278. https://dx.doi.org/10.1007/s11440-019-00874-y

81. Ziaei-Rad, V., Mollaali, M., Nagel, T., et al. (2022). Orthogonal decomposition of anisotropic constitutive models for the phase field approach to fracture. *Journal of the Mechanics and Physics of Solids*, 171: 105143. https://doi.org/10.1016/j.jmps.2022.105143

82. Ziefle, G., Cajuhi, T., Condamin, S., et al (2021). From process to system understanding with multi-disciplinary investigation methods: set-up and first results of the CD-A experiment (Mont Terri Rock Laboratory). *Safety of Nuclear Waste Disposal*, 1, pages 79–81. https://doi.org/10.5194/sand-1-79-2021

83. Ziefle, G., Cajuhi, T., Costabel, S., et al. (2023a). CD-A twin niches in the Mont Terri Rock Laboratory: Characterization and interpretation of hydraulic parameters with regard to safety aspects. *International Journal of Rock Mechanics and Mining Sciences*, 174: 105624. https://doi.org/10.1016/j.ijrmms.2023.105624

84. Ziefle, G., Cajuhi, T., Costabel, S., Furche, M., and Maßmann, J. (2024). Water content evolution in the EDZ of Opalinus Clay: A methodic approach for a comparative interpretation of measurements and modelling. *Rock Mechanics and Rock Engineering*. https://doi.org/10.1007/s00603-023-03717-1

85. Ziefle, G., Cajuhi, T., Graebling, N., et al. (2022). Multi-disciplinary investigation of the hydraulic-mechanically driven convergence behaviour: CD-A twin niches in the Mont Terri Rock Laboratory during the first year. *Geomechanics for Energy and the Environment*, 31: 100325. https://doi.org/10.1016/j.gete.2022.100325

86. Ziefle, G., Matray, J.-M., Maßmann, J., and Möri, A. (2018). Coupled hydraulic-mechanical simulation of seasonally induced processes in the Mont Terri rock laboratory (Switzerland). Swiss Journal of Geosciences, 110: 195-212. https://doi.org/10.1007/s00015-016-0252-1

87. Zienkiewicz, O. C., Chan, A. H. C., Pastor, M., et al. (1999). *Computational Geomechanics - With Special Reference to Earthquake Engineering*. John Wiley & Sons. ISBN: 0-471-98285-7